Finite-frequency-dependent noise of a quantum dot in a magnetic field

C. P. Moca
BME-MTA Exotic Quantum Phases Lendület Group, Institute of Physics, Budapest University of Technology and Economics, H-1521 Budapest, Hungary and Department of Physics, University of Oradea, 410087, Oradea, Romania

P. Simon
Laboratoire de Physique des Solides, CNRS UMR-8502, Université Paris Sud, 91405 Orsay Cedex, France

Chung-Hou Chung
Department of Electrophysics, National Chiao-Tung University, HsinChu, Taiwan, 300, Republic of China and Physics Division, National Center for Theoretical Science, Hsinchu, 30013, Taiwan, Republic of China

G. Zaránd
BME-MTA Exotic Quantum Phases Lendület Group, Institute of Physics, Budapest University of Technology and Economics, H-1521 Budapest, Hungary

(Received 20 December 2013; revised manuscript received 15 April 2014; published 29 April 2014)

We present a detailed study for the finite-frequency current noise of a Kondo quantum dot in the presence of a magnetic field by using a recently developed real-time functional renormalization group approach [C. P. Moca, P. Simon, C. H. Chung, and G. Zaránd, Phys. Rev. B **83**, 201303(R) (2011)]. The scaling equations are modified in an external magnetic field; the couplings and nonlocal current vertices become strongly anisotropic, and develop new singularities. Consequently, in addition to the natural emission threshold frequency, $\hbar\omega = |eV|$, a corresponding singular behavior is found to emerge in the noise spectrum at frequencies $\hbar\omega \approx |eV \pm B|$. The predicted singularities are measurable with present-day experimental techniques.

DOI: 10.1103/PhysRevB.89.155138 PACS number(s): 73.63.Kv, 72.15.Qm, 72.70.+m

I. INTRODUCTION

The study of out-of-equilibrium transport properties of correlated quantum systems is certainly one of the major challenges in condensed matter physics. Such correlated systems often emerge in mesoscopic physics and molecular electronics, and include, among others, real or artificial atoms and molecules, attached to several electrodes, which are typically set to different electrochemical potentials. Quantum dots (QDs)—realizing artificial atoms—represent the most basic building blocks of these devices. Once connected to conduction electrodes, they behave as artificial impurities interacting with the Fermi sea of conduction electrons on the electrodes attached. QDs with an odd number of electrons, in particular, realize artificial magnetic impurities, and thus typically display a Kondo effect, one of the most paradigmatic many-body phenomena in condensed matter systems.

Obviously, understanding time-dependent fluctuations in such nonequilibrium systems is of major importance. In this respect, the noise spectrum of a biased device is a very interesting and important quantity since it provides information on the dynamics of excitations on short-time scales. It is only very recently that it became possible to investigate high frequency noise and response functions in mesoscopic circuits in the quantum regime, $\hbar\omega \gg k_B T$ [1–3]. Thanks to progress in on-chip detection of high-frequency electronic properties, exploring the nonequilibrium fast dynamics of correlated nanosystems is now accessible, though experiments are delicate since they involve frequencies in the 30–100 GHz range [4]. In recent experiments, in particular, high frequency current fluctuations of a carbon nanotube quantum dot in the Kondo regime have been measured, by coupling the QD to a quantum detector via a superconducting resonant circuit [5]. Strong resonances have been observed in the emission noise for frequencies close to the bias voltage, in agreement with theoretical predictions [6,7].

Compared to experiments, theory is still lagging behind, and describing theoretically how such many-body states behave under nonequilibrium conditions represents a major unsolved challenge: though there are several approaches to describe electronic transport through correlated mesoscopic circuits [8–16], similarly to the approach presented here, currently none of them is able to describe these correlated states satisfactorily in all regimes of interest.

In this paper, we shall study the nonequilibrium noise spectrum of a generic strongly correlated mesoscopic element, a quantum dot. The description of time-dependent correlations is particularly challenging in this system, the reason being that the effective interaction between a QD and the conduction electrons cannot be treated perturbatively, and an infinite order resummation of the perturbative corrections is needed. For a nonequilibrium system, however, this resummation is especially complicated since the effective interaction does not only display a singularity at the Fermi energy $\omega \approx 0$, but also exhibits a singular structure whenever the transferred energy is in resonance with the chemical potential difference of the two electrodes, $\omega \approx |\mu_\alpha - \mu_\beta| = |eV_{\alpha\beta}|$. Simple-minded resummations where the frequency dependence of the effective coupling is neglected, cannot account for the aforementioned fine structure, and more sophisticated functional renormalization group schemes, similar to the ones used in Ref. [17] must be developed. Within the latter approach, however, the effective interaction becomes nonlocal in time, and the definition of instantaneous current operators satisfying current

conservation—and thus the computation of time-dependent correlation functions—becomes a particularly delicate issue [6]. It is probably for this reason that most calculations focused so far on the zero-frequency (shot-noise) limit [18–23], and finite-frequency results are rather limited [5,6,24–29].

In Ref. [6], we developed a current conserving real-time functional renormalization group (RG) formalism, and have shown that the somewhat intuitively derived equations of Ref. [30] follow easily within this formalism. We have shown that, similar to the effective interaction (vertex), local measurables (in time) also develop a nonlocal character in the course of the RG process. We then used this formalism to compute the noise spectrum of a quantum dot in the local moment regime [6] and compared that to the experimentally measured noise spectrum, to find good agreement [5]. Notice that our real-time FRG approach is different from the FRG approach used by Metzner *et al.* [31] and Kopietz *et al.* [32]; similar to the real-time RG of Schoeller and König [33], we work on the Keldysh contour, however, unlike the usual FRG method, we perform the RG transformation on the bare action and keep only quartic but nonlocal interaction terms.

Here, we intend to give a more detailed description of the formalism presented in Ref. [6] and extend it to the case where an external field is also present. Throughout this paper, we shall focus most of our attention on the Kondo model, where the external magnetic field B couples to the impurity spin operator $\mathbf{S}$,[1]

$$H_B = -BS^z ,$$

and the (unrenormalized) interaction is of a simple exchange form,

$$H_{\rm int} = \frac{1}{2}\sum_{\alpha,\beta\in L,R}\sum_{\sigma,\sigma'} j_{\alpha\beta}\ \psi^\dagger_{\alpha\sigma}\mathbf{S}\cdot\boldsymbol{\sigma}_{\sigma\sigma'}\psi_{\beta\sigma'} , \qquad (1)$$

with $\psi^\dagger_{\alpha\sigma}$ the creation operator of an electron of spin σ in lead $\alpha\in\{L,R\}$, $\boldsymbol{\sigma}$ the Pauli matrices, and the $j_{\alpha\beta}$ denoting dimensionless exchange couplings. Nevertheless, our formalism is very general and can be applied to any local quantum impurity problem with a "quantum impurity" having some internal quantum states, $s\in\{1,\ldots,Q\}$ of energy E_s and interacting with the leads through the Hamiltonian

$$H_{\rm int} = \sum_{i,k}\sum_{s,s'} g^{ss'}_{ik}\ |s\rangle\langle s'|\ \psi^\dagger_i\psi_k , \qquad (2)$$

with i and k labeling conduction electron channels of different chemical potentials, μ_i and μ_k, respectively.[2] The fields $\psi_{\alpha\sigma}$ (and ψ_i) in the previous equations are constructed in terms of quasiparticle operators,

$$\psi_{\alpha\sigma} = \int c_{\alpha\sigma}(\xi)e^{-|\xi|a/2}\,d\xi, \qquad (3)$$

with a a short time ($1/a$ a high energy) cutoff, and the operators $c_{\alpha\sigma}(\xi)$ destroying a quasiparticle of energy $\xi+\mu_\alpha$, in lead α (of energy $\xi+\mu_i$ in channel i in the general case).[3]

The nonequilibrium quantum impurity problems defined by Eqs. (1) and (2) constitute "hard problems" and do not possess complete solutions yet. The Kondo problem, Eq. (1) has, however, an exact solution under equilibrium conditions [34,35] and is well-understood [36–38]. For a quantum dot, in particular, the couplings $j_{\alpha\beta}$ assume the simple form, $j_{\alpha\beta} = j\ v^*_\alpha v_\beta$, with v_α a complex two-component spinor of unit length. The dimensionless coupling j generates a dynamical energy scale, the so-called Kondo temperature[4]

$$T_K \approx \frac{1.4}{a}\,e^{-1/j} .$$

Below this energy scale the effective exchange coupling becomes infinitely strong, and a local Kondo singlet is formed [36]. Similarly, in equilibrium, the effective couplings $g^{ss'}_{ik}$ of the generalized problem, Eq. (2) would typically scale to strong coupling below some Kondo scale provided that some of the levels E_s are degenerate.

Here, we shall not attempt to reach this strong coupling regime [7], rather we restrict ourself to the weak coupling regime, where either the voltage or the temperature, or the Zeeman splitting is sufficiently large compared to T_K. Our main goal is to investigate in detail the properties of the correlation functions of the current operators in this so-called "weak-coupling" regime and to determine the frequency-dependent conductance of a biased device as well as its emission/absorption noise spectrum and the symmetrized noise, accessible through direct measurements of the noise spectrum [2]. Particular attention shall be devoted to spin relaxation processes, which are crucial to provide a self-consistent cutoff to the singular structures. As we shall see, in a two-terminal Kondo device, all noise components exhibit interesting, singular structures at the thresholds $\omega=\pm eV$ and $\omega=\pm|eV\pm B|$. The differential emission noise spectrum $dS^{\rm em}(\omega)/dV$, in particular, exhibits a peak at $\omega\approx eV$ [5,6], which is then split in a magnetic field, as shown in Fig. 1, in agreement with the recent independent results of Ref. [39]. Similar structures are predicted in the symmetrized noise of the device (see Fig. 18).

The paper is organized as follows. In Sec. II, we introduce the real-time functional renormalization group formalism, with special emphasis on the construction of the Keldysh action and the derivation the scaling equations for the couplings. The current operator and the corresponding equations for the current vertices are discussed in Sec. III. In Sec. IV, we discuss the issue of decoherence in terms of the master equation approach and present results for the pseudofermion self-energy, while the result for the finite-frequency noise are presented in Sec. V. We give the final remarks in Sec. VI.

[1]We consider the effect of a local Zeeman field. A field applied to the conduction electrons has a similar effect.

[2]In the Kondo case, i is a composite label standing simultaneously for spin and lead indices $i=(\alpha,\sigma)$.

[3]The operators $c_{\alpha\sigma}(\xi)$ are normalized such that $\{c_{\alpha\sigma}(\xi),c^\dagger_{\alpha'\sigma'}(\xi')\} = \delta_{\alpha\alpha'}\delta_{\sigma\sigma'}\delta(\xi-\xi')$.

[4]The prefactor in the expression of T_K is not universal, and depends on the exponential cutoff scheme in Eq. (3). We determined it from the RG equations by identifying the energy at which the renormalized couplings diverge.

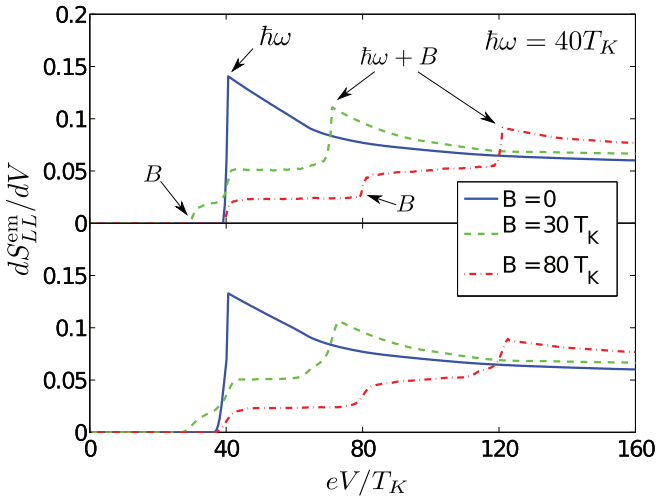

FIG. 1. (Color online) Voltage dependence of the differential emission noise, $dS^e_{LL}(V,T=0)/dV$ at a constant frequency, $\omega = 40\ T_K$ for various Zeeman splittings B. All energies are measured in units of the Kondo temperature, T_K. In the upper figure, the spin decay time has only been incorporated when computing the current vertex renormalization, while in the lower panel, a finite pseudofermion lifetime has been used to compute the diagrams in Fig. 14.

II. THE REAL-TIME FUNCTIONAL RENORMALIZATION GROUP APPROACH

In this section, we shall present in detail the real-time functional renormalization group (RTFRG) we have developed in Refs. [5] and [6]. First, we discuss how our functional RG formalism is constructed on the Keldysh contour and show how the RG equations of Ref. [9] can be derived within this formalism. Then, in the next section, we discuss how the RG equations can be extended to the current vertex (Sec. III B).

A. Keldysh action

For the nonequilibrium physics discussed here, it is most convenient to work with a path integral formalism on the Keldysh contour. This approach allows one to incorporate retardation effects in a natural way, and does not suffer from the restrictions of a Hamiltonian theory, where the renormalized theory is local. In this approach, fermionic fields are replaced by time-dependent Grassmann fields living on the Keldysh contour, $\psi^\dagger_{\alpha\sigma}(t) \to \overline{\psi}_{\alpha\sigma}(z)$, $(z \in K)$. As usual, the branches $z \to t_\pm = t \pm i\delta$ of the contour are labeled by a Keldysh label $\kappa = 1,2$, and they represent forward/backward propagations in time.

The dynamics of the systems is determined by the Keldysh action,

$$\mathcal{S} = \mathcal{S}_{\rm lead} + \mathcal{S}_{\rm spin} + \mathcal{S}_{\rm int}. \tag{4}$$

The terms $\mathcal{S}_{\rm lead}$ and $\mathcal{S}_{\rm spin}$ describe the conduction electrons action and the spin action in the absence of interaction. They are quadratic in the fields and determine the noninteracting Green's functions (see below).

The part $\mathcal{S}_{\rm spin}$ describes the spin, which we represent using Abrikosov's pseudofermions [40] as $S^i \to \frac{1}{2}\sum_{s,s'} f^\dagger_s \sigma^i_{ss'} f_{s'}$, with the pseudofermion operators $f^\dagger_s$ satisfying the constraint $\sum_s f^\dagger_s f_s \equiv 1$. Correspondingly, in the path integral language, the spin part of the Keldysh action simply reads

$$\mathcal{S}_{\rm spin} = \int_{z\in K} dz \sum_s \overline{f}_s(z)(-i\partial_z + \lambda_s) f_s(z)\,, \tag{5}$$

which can also be expressed in terms of the Keldysh labels κ as

$$\mathcal{S}_{\rm spin} = \sum_\kappa \int_{-\infty}^{\infty} dt \sum_s \overline{f}^{(\kappa)}_s(t)(-i\partial_t + s_\kappa \lambda_s) f^{(\kappa)}_s(t)\,, \tag{6}$$

with the sign s_κ being $s_\kappa = \pm$ for the upper ($\kappa = 1$) and lower ($\kappa = 2$) contours. Here, the chemical potentials $\lambda_s = \lambda_0 + sB/2$ account for the splitting of the two spin states, $s = \pm$, but they also act as Lagrange multipliers to implement the constraints, and allow us to separate in the $\lambda_0 \to \infty$ limit the contribution of the states satisfying $\sum_s f^\dagger_s f_s \equiv 1$. The actions (5) and (6) determine the four pseudofermion correlation functions $F^{t/\bar t}_s$ and $F^{\gtrless}_s$ depending on the choice of the Keldysh branches κ and κ' (see Appendix). The time-ordered propagator, e.g., is given by the "11" component, $F^t_s(t) = F^{(11)}_s(t)$,

$$\begin{aligned} F^{(11)}_s(t) &= -i\left\langle f^{(1)}_s(t)\overline{f}^{(1)}_s(0)\right\rangle_{\mathcal{S}_{\rm spin}} = -i\langle T_t f_s(t) f^\dagger_s(0)\rangle \\ &\approx -i\, e^{-i\lambda_s t}(\Theta(t) - e^{-\beta\lambda_s}\overline{\Theta}(t)), \end{aligned} \tag{7}$$

with T_t denoting the time ordering and $\Theta(t)$ and $\overline{\Theta}(t) = 1 - \Theta(t)$ the forward and backward step functions, respectively.

The interaction part of the action, $\mathcal{S}_{\rm int}$, is initially local in time. However, as we shall see, the elimination of high-energy degrees of freedom—implemented in our scheme by rescaling a in Eq. (3)—generates retardation effects in the course of the RG procedure and the interaction becomes therefore *nonlocal* in time. We therefore replace the Kondo couplings by some time-dependent vertex functions, $g^{\sigma s;\sigma' s'}_{\alpha\alpha'}(t)$, which depend on the incoming and outgoing electrons' spin and lead indices and on the pseudofermion spins, and write the interacting part of the action as

$$\begin{aligned} \mathcal{S}_{\rm int} = \sum_\kappa \sum_{\alpha\alpha'\sigma\sigma'} \sum_{s,s'} \int dt\, dt'\, s_\kappa\, g^{\sigma s;\sigma' s'}_{\alpha\alpha'}(t-t') \\ \times \bar f^{(\kappa)}_s(\bar t) f^{(\kappa)}_{s'}(\bar t)\cdot \bar\psi^{(\kappa)}_{\alpha\sigma}(t)\psi^{(\kappa)}_{\alpha'\sigma'}(t')\,. \end{aligned} \tag{8}$$

Here, $\bar t = (t+t')/2$, and the tensor function $g^{\sigma s;\sigma' s'}_{\alpha\beta}(t)$ collects the various components of the Kondo couplings. Initially, the couplings $g^{\sigma s;\sigma' s'}_{\alpha\beta}(t)$ are local in time and are given by

$$g^{\sigma s;\sigma' s'}_{\alpha\alpha'}(t) = \frac{j_{\alpha\alpha'}}{4}\,\boldsymbol{\sigma}_{ss'}\cdot\boldsymbol{\sigma}_{\sigma\sigma'}\,\delta(t)\,. \tag{9}$$

In the absence of an external field, this SU(2) invariant structure is conserved, $g^{\sigma s;\sigma' s'}_{\alpha\alpha'}(t) \to (g_{\alpha\alpha'}(t)/4)\,\boldsymbol{\sigma}_{ss'}\cdot\boldsymbol{\sigma}_{\sigma\sigma'}$, and it is enough to keep track of just four functions, $g_{\alpha\alpha'}(t)$ [see also Eq. (18)].

The structure in Eq. (8) can be justified by observing that the spin evolves very slowly at electronic time scales and interacts only weakly with the electrons. Therefore its time evolution can be well approximated by that of a free spin (pseudofermion). In contrast, conduction electrons have fast dynamics, and their scattering on the slow impurity

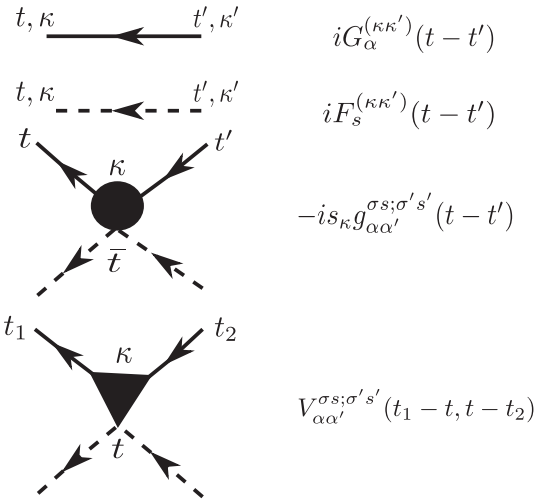

FIG. 2. Components of real-time Feynman diagrams. Electron and pseudofermion propagators are denoted by continuous and dashed lines, respectively. Incoming and outgoing electrons carry Keldysh (κ), spin (σ), and lead (α) quantum numbers, while pseudofermions carry only Keldysh and spin (s) labels. The nonlocal vertex $g_{\alpha\beta}^{\sigma s;\sigma' s'}(t)$ is indicated by a filled circle. The time argument of the pseudofermion is $\bar{t}=(t+t')/2$. Finally, the current vertex is labeled by three time arguments: the time t of the measurement, and the times t_1 and t_2 of the incoming and outgoing electrons.

spin induces retardation effects which become more and more pronounced as one approaches smaller and smaller energy scales or, equivalently, long-time scales. These are precisely the effects we want to capture within our formalism. Technically, this implies that we need to keep the time arguments of the electron fields $\overline{\psi}_{\alpha\sigma}(t)$ and $\psi_{\alpha'\sigma'}(t')$, while we can eliminate the time evolution of the pseudofermion fields using their bare real-time evolution, $f_s(t)\approx e^{-i\lambda_s(t-t')}f_s(t')$ for short time differences. From a diagrammatic point of view, we can represent the interaction term (8) by a nonlocal vertex diagram, depicted in Fig. 2.

Notice that the couplings in (8) do not have a Keldysh label, and that all fields live on the same branch of the Keldysh contour. This is obvious for the bare action, but this structure is also approximately maintained by the renormalized action as long as only singular terms are summed up (see Sec. II B).

Finally, the term $\mathcal{S}_{\rm lead}$ describes the electrons in the leads and generates the noninteracting Keldysh Green's functions of the fields $\psi_{\alpha\sigma}(t)$. At $T=0$ temperature, e.g., a simple calculation yields for the time-ordered and greater propagators

$$\begin{aligned}G^{t}_{\alpha\sigma;\alpha'\sigma'}(t)&=-i\langle T_t\psi_{\alpha\sigma}(t)\psi^{\dagger}_{\alpha'\sigma'}(0)\rangle\\&=\delta_{\alpha\alpha'}\delta_{\sigma\sigma'}G^{t}_{\alpha}(t)=\frac{-\delta_{\alpha\alpha'}\delta_{\sigma\sigma'}e^{-i\mu_\alpha t}}{t-ia\ \mathrm{sgn}(t)},\\G^{>}_{\alpha\sigma;\alpha'\sigma'}(t)&=-i\langle\psi_{\alpha\sigma}(t)\psi^{\dagger}_{\alpha'\sigma'}(0)\rangle\\&=\delta_{\alpha\alpha'}\delta_{\sigma\sigma'}G^{>}_{\alpha}(t)=\frac{-\delta_{\alpha\alpha'}\delta_{\sigma\sigma'}e^{-i\mu_\alpha t}}{t-ia}.\end{aligned}$$

The other electronic propagators are given by similar expressions and are listed in Appendix.

B. Derivation of the RG equations for the couplings

Let us now turn to the derivation of the RG equations. In this section, we shall proceed by using Wilson's RG approach within a path integral formalism [41]: we gradually increase the time scale $a\to a'$ thereby eliminating high energy electronic degrees of freedom, and compensate for the reduction of the cutoff $1/a\to 1/a'$ by renormalizing the vertex function $\boldsymbol{g}(t)\to\boldsymbol{g}'(t)$.

To determine the renormalization of $\boldsymbol{g}(t)$, let us assume an interaction vertex of the form (8) and expand the functional

$$\mathcal{Z}\equiv\int\mathcal{D}f\mathcal{D}\overline{f}\int\mathcal{D}\psi\mathcal{D}\overline{\psi}\ e^{-iS}$$

in $\mathcal{S}_{\rm int}$. The contributions of nth-order diagrams can be evaluated using Wick's theorem, and can be represented by Feynman diagrams. The diagrammatic components are shown in Fig. 2.

It is relatively easy to see that, as a result of the structure of the pseudofermion Green's functions listed in Appendix, each pseudofermion loop contains at least one exponentially small pseudofermion propagator, $\sim e^{-\beta\lambda_s}$, since for any time configuration it involves at least one of the three propagators, $F_s^{<}(t)$, $F_s^{t}(t<0)$, or $F_s^{\bar{t}}(t>0)$. The physical subspace, however, corresponds to having *exactly* one pseudofermion, which has a probability $P_1=\sum_s e^{-\beta\lambda_s}$. In fact, when computing physical quantities, the contribution of every diagram must be normalized by this probability, while the chemical potential of the pseudofermions is taken to infinity, $\lambda_s\to\infty$. Thus the physical subspace $\sum_s f_s^{\dagger}f_s=1$ corresponds to diagrams with a single time-ordered pseudofermion loop.

It follows by the same argument that, upon integration over all time arguments of a given diagram, only those time configurations give a contribution where the pseudofermion lines are time ordered along the Keldysh loop (see Fig. 3). The pseudofermion fields thus lead to an effective time ordering along the Keldysh contour. The contribution of all diagrams in Fig. 3 is thus proportional to $\sim e^{-\beta\lambda_s}$, which is, as explained above, proportional to the probability of

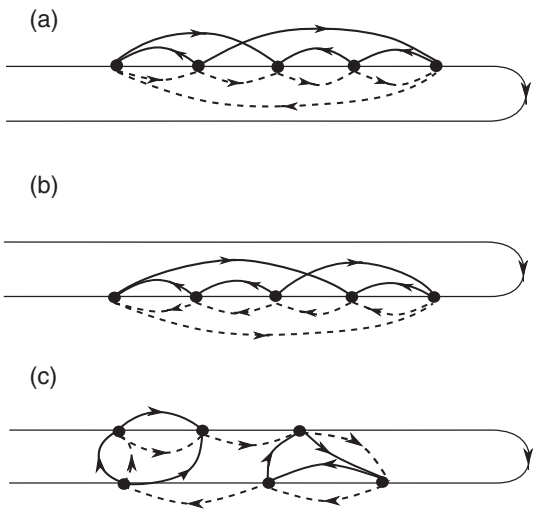

FIG. 3. The physical subspace $\sum_s f_s^{\dagger}f_s=1$ corresponds to diagrams with a single time-ordered pseudofermion loop.

having exactly one pseudofermion available. Of course, time ordering is automatically performed by the Θ functions in the pseudofermion propagators, upon integration over all internal time arguments of a given diagram.

Let us now investigate the effect of changing $a \to a' = a + \delta a$. In a given nth-order diagram, we need to perform $2n$ integrations over some times on the upper and on the lower contour. However, under the rescaling $a \to a'$ the value of the integrand changes substantially only when two of the contracted time arguments of the fields $\psi^{(\kappa)}_{\alpha\sigma}$, say t_1 and t_2 happen to be close to each other, $|t_{12}| \equiv |t_1 - t_2| \sim a$, implying that all time arguments of the two corresponding vertices must also be close to each other. This is obvious from the structure of the fermionic Green's functions, which change only locally upon rescaling $a \to a'$. The change in $G^t_\alpha(t_1 - t_2)$ is, e.g., approximately equal to

$$\delta G^t_\alpha(t_{12}) \approx -ie^{-i\mu_\alpha t_{12}} \frac{\delta a\ \mathrm{sgn}(t_{12})}{(t_{12} - ia\ \mathrm{sgn}(t_{12}))^2}$$

at $T = 0$ temperature, and decays asymptotically as $\mathrm{sgn}(t_{12})/t^2_{12}$. Similarly, the rescaling of any other electronic Green's function gives a short range contribution in time. Therefore we can safely assume that the typical distance of $t_1 \approx t_2$ from the time arguments of all other vertices is large compared to $|t_1 - t_2| \sim a$. Under this assumption, we can integrate over contracted local time arguments, t_1 and t_2, and compensate the change $\delta G^{(\kappa\kappa')}_\alpha$ by adding a corresponding interaction term to the action.

Let us now focus on two vertices as being part of a big diagram containing $n > 2$ vertices. Using Wick's theorem, we can write the contribution of these two vertices as a sum of normal ordered operators (which contain fields f, $\overline{f}$, ψ, $\overline{\psi}$ to be contracted with external vertices) multiplied by certain internal contractions. Typical contractions are sketched in Fig. 4. We only show those contractions that contain at least one ψ contraction, since only these contributions change upon rescaling a, and therefore only these diagrams can give a contribution to the renormalized action, at least in leading order in a. Furthermore, as a basic principle, we shall keep only those diagrams that do not vanish in the equilibrium limit, $B \to 0$ and $\mu_L = \mu_R$.

We have the following four classes. (a) Diagrams with a single ψ contraction. Such diagrams do not give a contribution for the following reasons. If one of the vertices is on contour $\kappa = 1$ and the other on contour $\kappa' = 2$, then its change is proportional to $\delta G^{\gtrless}(t_1 - t_2) \sim 1/(t_{12} \pm i\,a)^2$. The strength of this correction can be estimated within the local approximation, $\boldsymbol{g}(t) \to \boldsymbol{g}\,\delta(t)$, whereby one replaces the fields $\bar\psi(t) \to \bar\psi(\bar t)$ and $\psi(t') \to \psi(\bar t)$, and integrates over the internal variable, t_{12}. This procedure yields a vanishing contribution. If, on the other hand, the two vertices are on the same Keldysh branch, then at least one pseudofermion leg of the two vertices must be connected. This follows from the observation that, to give a nonvanishing (i.e., $\sim e^{-\beta\lambda_0}$) contribution, the time arguments of the pseudofermions must be contracted to form an ordered loop along the contour. Diagrams of type (a) can thus be ignored. (b) and (b') Diagrams with one pseudofermion line contraction and one ψ contraction. These diagrams renormalize $\boldsymbol{g}$, as shall be discussed in detail below. (c) Diagrams with two ψ contractions. These diagrams account for the relaxation of the spin's density matrix, and incorporate information on the Korringa relaxation. We shall neglect these diagrams, and only keep track of the spin relaxation through the pseudofermion's relaxation [diagram (d)]. (d) Diagrams with two ψ contractions and one pseudofermion contraction. These diagrams generate a pseudofermion self-energy, and account for (at least part of the) spin relaxation.

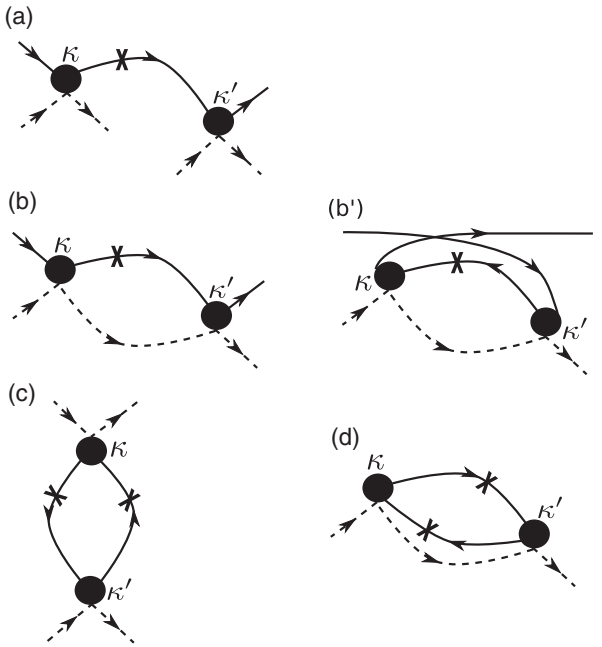

FIG. 4. Possible contractions of two vertices with time arguments at a distance $\sim a$. Contractions of type (b) and (b') renormalize the interaction, while contractions of type (d) renormalize the pseudofermion propagators and account for spin relaxation. Crosses indicate the logarithmic derivative with respect to the scaling parameter a.

Let us now focus on the vertex renormalization, i.e., on the family of diagrams (b) and (b') in Fig. 4. Depending on the Keldysh labels of the two vertices, these give rise to $4 + 4$ diagrams, as shown in Fig. 5. As an example, let us discuss the first diagram (diagram (1) in Fig. 5), on the upper Keldysh contour. By rescaling a, we generate the following term in the effective action:

$$\begin{aligned} -i\mathcal{S}^{(1)}_{\mathrm{int}} = \int dt\,dt' \sum_{\alpha,\alpha',\sigma,\sigma'} \sum_{s,s'} \Bigg\{ \sum_{\tilde\alpha,\tilde s,\tilde\sigma} \int dt_1\,dt_2\, g^{\sigma\tilde\sigma;s\tilde s}_{\alpha\tilde\alpha}(t - t_1) \\ \times g^{\tilde\sigma\sigma';\tilde s s'}_{\tilde\alpha\alpha'}(t_2 - t')\delta G^t_{\tilde\alpha}(t_1 - t_2) \\ \times F^t_{\tilde s}\left[\frac{1}{2}(t + t_1 - t_2 - t')\right] e^{i\lambda_s(t_1 - t')/2}\, e^{-i\lambda_{s'}(t_2 - t)/2} \Bigg\} \\ \times \bar f^{(1)}_s(\bar t) f^{(1)}_{s'}(\bar t) \cdot \bar\psi^{(1)}_{\alpha\sigma}(t)\psi^{(1)}_{\alpha'\sigma'}(t'), \end{aligned} \tag{10}$$

where $\bar t = (t + t')/2$. In order to obtain this equation, we have used the expansion

$$\bar f^{(1)}_s\left(\frac{t + t_1}{2}\right) \approx \bar f^{(1)}_s(\bar t)\, e^{i\lambda_s(t_1 - t')/2} \quad \text{and}$$

$$f^{(1)}_{s'}\left(\frac{t_2 + t'}{2}\right) \approx f^{(1)}_{s'}(\bar t)\, e^{-i\lambda_{s'}(t_2 - t)/2},$$

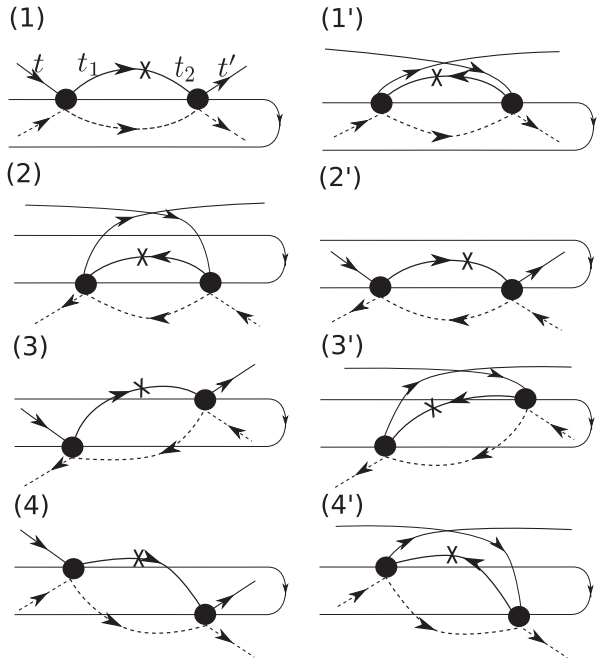

FIG. 5. Possible vertex corrections. To leading order, only diagrams (1), (1'), (2), and (2') contribute to vertex renormalization. Crosses indicate the logarithmic derivative with respect to the scaling parameter a.

which assumes a slow spin dynamics compared to that of the electrons. We thus conclude that we can compensate for the change of the Green's function δG^t_α in diagrams of type (1) in Fig. 5 by renormalizing the interaction kernel $g(t)$ on the upper Keldysh contour by

$$\delta g^{(1)}(t-t') = \sum_{\tilde\alpha,\tilde s,\tilde\sigma} \int dt_1\, dt_2\, g^{\sigma s;\tilde\sigma\tilde s}_{\alpha\tilde\alpha}(t-t_1) g^{\tilde\sigma\tilde s;\sigma' s'}_{\tilde\alpha\alpha'}(t_2-t') \times \delta G^t_{\tilde\alpha}(t_1-t_2) F^t_{\tilde s}\left[\frac{1}{2}(t+t_1-t_2-t')\right] \times \exp\left[i\frac{\lambda_s}{2}(t_1-t')\right]\exp\left[-i\frac{\lambda_{s'}}{2}(t_2-t)\right]. \tag{11}$$

The contributions of the other diagrams can be treated similarly. However, while diagrams (1), (1'), (2), and (2') lead to changes of time- and anti-time-ordered electronic propagators $\sim \mathrm{sgn}\, t_{12}/(t_{12} \pm ia\, \mathrm{sgn}\, t_{12})^2$, integrating to a finite value $\sim 1/a$, changing the electron propagators in diagrams (3), (3'), (4), and (4') results in terms $\sim 1/(t_{12} \pm ia)^2$, and integrate to ≈ 0. Notice that in the latter four diagrams the pseudofermion propagators do not contain Θ functions. Therefore these diagrams do not result in any interesting renormalization. Put in another way, the parent diagrams of (1), (1'), (2), and (2') (without the crosses) contain *logarithmic singularities* associated with the contraction of t_1 and t_2, while the diagrams (3), (4), and (4') contain no such singularity. In the spirit of leading logarithmic approximation, where only maximally singular diagrams are kept, we thus drop the latter two sets of diagrams. Notice that within this approximation, the generated vertex functions do *not have* off-diagonal Keldysh

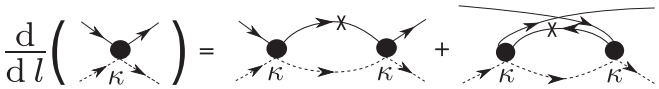

FIG. 6. Graphical representation of Eq. (12). The derivatives with respect to a of the electronic Green's functions are represented by crossed solid lines.

labels. Furthermore, one can show that the contributions of diagrams (3) and (4) are identical to those of (1) and (2), and therefore the structure of Eq. (8) is conserved by the RG procedure. The renormalized coupling, g' can thus be expressed as $g' = g + \delta g$, with $\delta g = \delta g^{(1)} + \delta g^{(1')}$, and with $\delta g^{(1')}(t-t')$ given by an expression similar to (11). Introducing the scaling variable $l = \ln(a/a_0)$ and then dividing δg by $\delta a/a = \delta l$, we obtain an integro-differential equation for the coupling $g(t-t')$:

$$\frac{dg(t-t')}{dl} = \sum_{\tilde\alpha,\tilde s,\tilde\sigma} \int dt_1\, dt_2 \Big[g^{\sigma s;\tilde\sigma\tilde s}_{\alpha\tilde\alpha}(t-t_1) g^{\tilde\sigma\tilde s;\sigma' s'}_{\tilde\alpha\alpha'}(t_2-t') \times \frac{\partial G^t_{\tilde\alpha}(t_1-t_2)}{\partial l} F^t_{\tilde s}\left(\frac{t+t_1-t_2-t'}{2}\right) \times e^{i\lambda_s(t_1-t')/2} e^{-i\lambda_{s'}(t_2-t)/2} + g^{\sigma\tilde s;\tilde\sigma s'}_{\alpha\tilde\alpha}(t-t_1) g^{\tilde\sigma s;\sigma'\tilde s}_{\tilde\alpha\alpha'}(t_2-t') \frac{\partial G^t_{\tilde\alpha}(t_1-t_2)}{\partial l} \times F^t_{\tilde s}\left(\frac{t'+t_2-t_1-t}{2}\right) e^{i\lambda_s(t_2-t)/2} e^{-i\lambda_{s'}(t_1-t')/2} \Big]. \tag{12}$$

This constitutes a complete integro-differential equation for the vertex function with the boundary conditions (9). It can be represented graphically as in Fig. 6. As we have discussed, during the RG procedure one generates pseudofermion self-energy corrections [diagrams (d) in Fig. 4]. The imaginary part of these self-energy corrections corresponds to pseudofermion decay, and is proportional to the spin relaxation rate (see Sec. IV). Equation (12) thus incorporates spin relaxation through the pseudofermion propagators F^t_s.

Fortunately, these somewhat cumbersome equations can be further simplified by relatively simple approximations. At $T = 0$ temperature, the pseudofermion propagator F^t_s is approximately given by

$$F^t_{\tilde s}\left(\frac{t+t_1-t_2-t'}{2}\right) \approx -i\Theta\left(\frac{t+t_1-t_2-t'}{2}\right) e^{-i(t+t_1-t_2-t')\lambda_{\tilde s}/2}. \tag{13}$$

If we assume that typical electronic time differences involved in the vertices are short compared to $t_1 - t_2$, we can then set $t \to t_1$ and $t' \to t_2$ in the argument of the Θ function, giving $\Theta(t_1 - t_2)$. With this approximation, the exponential functions can be regrouped and time integrals become simple convolutions. In this spirit, we approximate $F^t_{\tilde s}$ as

$$bF^t_{\tilde s}\left(\frac{t+t_1-t_2-t'}{2}\right) \approx \left[F^t_{\tilde s}(t_1-t_2) e^{i(t_1-t_2)\lambda_{\tilde s}}\right] e^{-i(t+t_1-t_2-t')\lambda_{\tilde s}/2}. \tag{14}$$

Writing furthermore $G^t_\alpha(t)$ as $G^t_\alpha(t) = G^t_0(t)e^{-i\mu_\alpha t}$ and thus separating its trivial chemical potential dependence, the above integro-differential equations reduce to the following differential equations in Fourier space:

$$\frac{d\, g^{\sigma s;\sigma' s'}_{\alpha\alpha'}(\omega)}{dl} = \sum_{\tilde\alpha\tilde\sigma\tilde s}\Bigg[g^{\sigma s;\tilde\sigma s'}_{\alpha\tilde\alpha}\left(\omega + \frac{\lambda_{\tilde s s}}{2}\right) g^{\tilde\sigma s;\sigma' \tilde s}_{\tilde\alpha\alpha'}\left(\omega + \frac{\lambda_{\tilde s s'}}{2}\right) \times \Xi^{\tilde s}_a\left(\omega - \frac{\lambda_{s\tilde s} + \lambda_{s'\tilde s}}{2} - \mu_{\tilde\alpha}\right) - g^{\sigma s;\tilde\sigma\tilde s}_{\alpha\tilde\alpha}\left(\omega + \frac{\lambda_{s'\tilde s}}{2}\right) g^{\tilde\sigma\tilde s;\sigma' s'}_{\tilde\alpha\alpha'}\left(\omega + \frac{\lambda_{s\tilde s}}{2}\right) \times \Xi^{\tilde s}_a\left(\omega + \frac{\lambda_{s\tilde s} + \lambda_{s'\tilde s}}{2} - \mu_{\tilde\alpha}\right)\Bigg], \tag{15}$$

where the notation $\lambda_{ss'} = \lambda_s - \lambda_{s'}$ has been introduced for the energy splitting of the states s and s'. The cutoff function $\Xi^s_a(\omega)$ can be expressed here as

$$\Xi^s_a(\omega) = -\int dt\, e^{i\omega t} F^t_s(t)\, e^{it\lambda_s} \frac{\partial G^t_0(t)}{\partial l}. \tag{16}$$

This function, on the one hand, accounts for the finite bandwidth of the conduction electrons, and cuts off contributions at frequencies $|\omega| \gtrsim 1/a$. However, it also accounts for the finite temperature thermal decoherence of the conduction electrons at times $t > 1/T$, and furthermore, also incorporates the effect of spin relaxation processes through the pseudofermion propagator F^t. For most practical purposes the detailed shape of this cutoff function is not very relevant, and for practical purposes it can usually be replaced by a simple function

$$\Xi^s_a(\omega) \approx \Theta[1/a - (\omega^2 + \Gamma^2)^{1/2}], \tag{17}$$

with $\Gamma = \Gamma(a)$ a spin relaxation rate that we determine self-consistently (for details, see Sec. IV). The validity of these latter approximations can be checked against the solution of the full integro-differential equations (12). We emphasize that relaxation processes play an important role since even at $T = 0$ temperature a finite bias voltage can generate a large intrinsic spin relaxation, Γ, which regularizes the logarithmic singularities. The scaling equations (15) are valid in the presence of the external magnetic field which enters through the pseudofermions energy $\lambda_s = \lambda_0 - sB/2$, $(s = \pm 1)$. At the same time, they are identical to the equations obtained in a more heuristic way in Refs. [42] and [30]. However, in our real-time functional RG formalism, the derivation is rather straightforward and the approximations made are better controlled.

Notice that the usual poor man's RG procedure can be recovered by the local approximation, i.e., by dropping the time dependence of g, and replacing the generated nonlocal couplings by local ones, $\mathbf{g}(t) \to \delta(t) \int dt\, \mathbf{g}(t)$, which corresponds to assuming frequency independent couplings in Eq. (15).

In the absence of an external magnetic field, all couplings are of the form

$$g^{\sigma s;\sigma' s'}_{\alpha\alpha'}(t) = \tfrac{1}{4}\, \boldsymbol{\sigma}_{ss'} \cdot \boldsymbol{\sigma}_{\sigma\sigma'}\, g_{\alpha\alpha'}(t)\,, \tag{18}$$

the terms $\lambda_{ss'}$ identically vanish, and and the renormalization group equations simplify to

$$\frac{d\, g_{\alpha\alpha'}(\omega)}{dl} = \sum_{\tilde\alpha} g_{\alpha\tilde\alpha}(\omega)\; g_{\tilde\alpha\alpha'}(\omega)\, \Xi_a(\omega - \mu_{\tilde\alpha})\,. \tag{19}$$

We determine the renormalized couplings by solving Eq. (15) [or Eq. (19)] numerically, while taking into account the spin decoherence rate [see Sec. IV and, particularly, Eq. (34)]. As discussed in the introduction, the initial couplings $j_{\alpha\beta}$ can be parametrized in terms of a single dimensionless coupling, j, and a spinor v_α. It is convenient to choose a suitable gauge so that v_α is real, and can be parametrized in terms of a single angle θ, as $\{v_\alpha\} = \{\cos(\theta/2), \sin(\theta/2)\}$. In terms of this, the matrix $j_{\alpha\beta}$ becomes

$$\mathbf{j} = \begin{pmatrix} j_{LL} & j_{LR} \\ j_{RL} & j_{RR} \end{pmatrix} = j \begin{pmatrix} \cos^2\frac{\theta}{2} & \cos\frac{\theta}{2}\sin\frac{\theta}{2} \\ \cos\frac{\theta}{2}\sin\frac{\theta}{2} & \sin^2\frac{\theta}{2} \end{pmatrix}. \tag{20}$$

The value $\theta = \pi/2$ corresponds to symmetrical coupling to the left and right electrodes, while for $\theta = \pi$ and $\theta = 0$ the quantum dot is decoupled from the left and right electrode, respectively.

Typical results for some of the components of the matrix $\mathbf{g}(\omega)$ are displayed in Fig. 7. The rescaled couplings display strong features (logarithmic singularities in the absence of decoherence) at frequencies of the order of voltage drop between the external contacts, $\omega = \pm V/2$. The effect of the

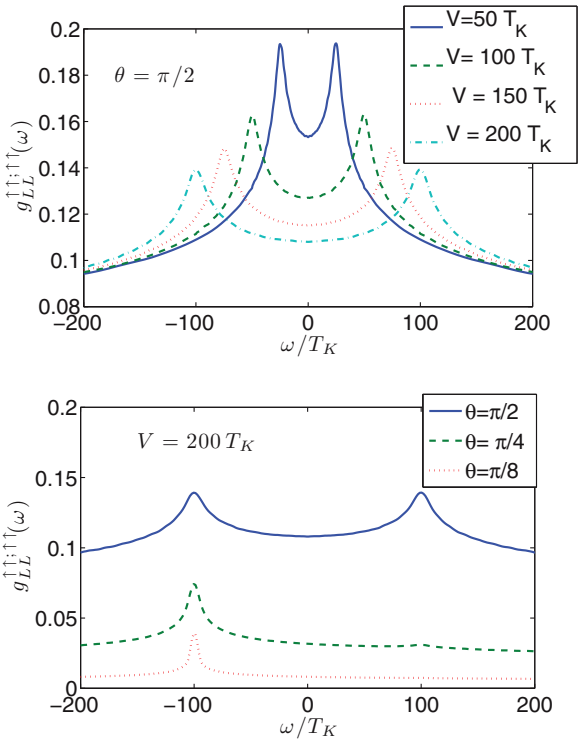

FIG. 7. (Color online) (Top) The frequency dependence of the $g^{\uparrow\uparrow;\uparrow\uparrow}_{LL}(\omega)$ component of the coupling matrix for different voltage biases. The magnetic field is set to zero. (Bottom) The frequency dependence of the same component for a fixed bias $V = 200\, T_K$, but for different θ. Spin relaxation has been incorporated self-consistently (see text).

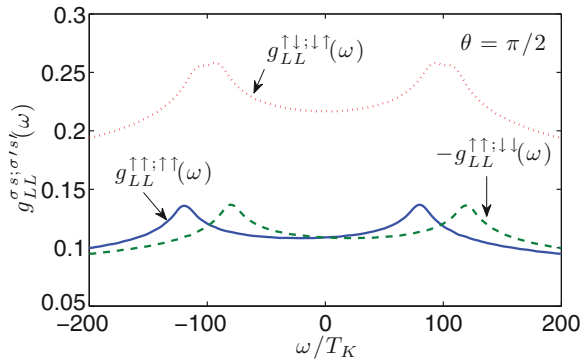

FIG. 8. (Color online) The frequency dependence of the nonzero components of the coupling matrix in an external magnetic field $B = 20\,T_K$. The voltage bias is fixed to $V = 200\,T_K$.

asymmetry on the renormalized couplings is shown in Fig. 7. Notice that for strong asymmetry ($\theta \approx 0$ or $\approx\pi$), only the peak associated with the Fermi surface of the more strongly coupled electrode survives, while the other is almost washed away. The effect of the magnetic field on the renormalized couplings is presented in Fig. 8. The longitudinal couplings $g^{\sigma s;\sigma s}_{\alpha\beta}(\omega)$ develop peaks at $\omega = \pm V/2 - \sigma B$, while the transversal ones $g^{\sigma\bar{\sigma};\bar{\sigma}\sigma}_{\alpha\beta}(\omega)$ develop peaks at at $\pm 1/2(V \pm B)$. Notice that the decoherence rate Γ prevents the flow from running towards the strong coupling regime. Therefore the peaks in the renormalized couplings get slightly broader and partially suppressed.

III. SCALING EQUATIONS FOR THE CURRENT VERTEX OPERATOR

A. Current and noise definitions

Having established the RG equations for the interaction vertex, let us now turn to the definition and renormalization of the current operator. The current operator can be constructed by exploiting the equations of motion, and take on forms similar to Eqs. (1) and (2). In the Kondo model, one trivially finds

$$\hat{I}_L(t) = -\hat{I}_R(t) = \sum_{\alpha\beta} \frac{e}{2} v^L_{\alpha\beta}\, \mathbf{S}(t)\cdot \psi^\dagger_\alpha(t)\boldsymbol{\sigma}\psi_\beta(t)\,, \tag{21}$$

with the time arguments indicating Heisenberg operators. Here, for simplicity, we suppressed the internal spin indices and expressed the current vertex matrices as

$$\mathbf{v}^L \equiv \mathbf{v} = -\mathbf{v}^R = \begin{pmatrix} 0 & -ij_{LR} \\ ij_{LR} & 0 \end{pmatrix}. \tag{22}$$

In the Kondo model, current conservation is satisfied at the operator level, $\hat{I}_L(t) = -\hat{I}_R(t)$. For the general Hamiltonian, (2), the equation of motion amounts to a similar expression of the form,

$$\hat{I}_k(t) = \sum_{m,n,s,s'} e\,[v^k]^{ss'}_{mn} X_{ss'}(t)\psi^\dagger_m\psi_n(t)\,, \tag{23}$$

with the $X_{ss'}(t)$ denoting time evolved Hubbard operators, $|s\rangle\langle s'|$, and the current vertices given by

$$[v^{(k)}]^{ss'}_{mn} = -i\,(\delta_{mk} - \delta_{nk}) g^{ss'}_{mn}\,. \tag{24}$$

Having the current operators at hand, one can then define the various current-current correlation functions. The "bigger" and "lesser" noise correlation functions are defined as

$$S^{>}_{\alpha\beta}(t,t') = \langle \hat{I}_\alpha(t)\,\hat{I}_\beta(t')\rangle \quad \text{and} \tag{25}$$

$$S^{<}_{\alpha\beta}(t,t') = \langle \hat{I}_\alpha(t')\,\hat{I}_\beta(t)\rangle, \tag{26}$$

while the symmetrized and antisymmetrized noise components are given by

$$S^{s/a}_{\alpha\beta}(t,t') = \tfrac{1}{2}\langle [\hat{I}_\alpha(t)\,,\hat{I}_\beta(t')]_\pm\rangle, \tag{27}$$

with $[\ldots,\ldots]_\pm$ denoting anticommutators/commutators, respectively. The Fourier spectra of these are directly accessible through noise measurements. The spectra of $S^{\gtrless}(\omega)$ can be measured by emission or absorption experiments [43,44], while the symmetrized noise is accessible through standard ac noise spectroscopy. [2,45].

B. Current vertex scaling equations

Having established the RG equations for the interaction vertex, let us now turn to the renormalization of the current operator. To compute the current-current correlation functions (26) and (27) within the path integral formalism, we first express the current operators $\hat{I}_\alpha$ in terms of Grassmann fields on the Keldysh contour, $\hat{I}_\alpha \to I^{(\kappa)}_\alpha$. Representing the spin operators using pseudofermions, we obtain

$$\hat{I}_\alpha \to I^{(\kappa)}_\alpha(t) = \sum_{\alpha\alpha'\sigma\sigma' ss'} \frac{e}{4} v^\alpha_{\alpha\alpha'} \bar{f}^{(\kappa)}_s(t)\boldsymbol{\sigma}_{ss'} f^{(\kappa)}_{s'}(t) \times \bar{\psi}^{(\kappa)}_{\alpha\sigma}(t)\boldsymbol{\sigma}_{\sigma\sigma'}\psi^{(\kappa)}_{\alpha'\sigma'}(t)\,. \tag{28}$$

Introducing then the corresponding generating functional,

$$Z\big[h^{(\kappa)}_\alpha(t)\big] \equiv \Big\langle e^{-i\,\sum_{\alpha=L,R}\sum_\kappa \int dt\, h^{(\kappa)}_\alpha(t) I^{(\kappa)}_\alpha(t)}\Big\rangle_{\mathcal{S}}\,, \tag{29}$$

all current-current correlation functions can be generated by functional differentiation with respect to $h_\alpha(t)$.

Unfortunately, however, similar to the interaction vertex $\boldsymbol{g}$, the current vertex becomes nonlocal in time upon rescaling $a \to a'$, and therefore Eq. (28) only holds for the unrenormalized (bare) current operator. Also, though the current vertex is initially obviously related to the interaction vertex, its generated time structure turns out to be very different from that of the interaction vertex and, as we show later, it necessarily acquires the following form under the RG

$$I_L(t) = e\sum_{\alpha\alpha'}\sum_{\sigma\sigma' ss'}\int dt_1\,dt_2\,(V^L)^{\sigma s;\sigma' s'}_{\alpha\alpha'}(t_1 - t, t - t_2) \times \bar{f}_s(t) f_{s'}(t)\cdot \bar{\psi}_{\alpha\sigma}(t_1)\psi_{\alpha'\sigma'}(t_2) \tag{30}$$

with the initial condition that for the bare theory, $a = a_0$

$$(V^L)^{\sigma s;\sigma' s'}_{\alpha\alpha'}(\tau_1,\tau_2,a_0) = \tfrac{1}{2}\delta(\tau_1)\,\delta(\tau_2)\,v^L_{\alpha\beta}\,\boldsymbol{\sigma}_{\sigma\sigma'}\mathbf{S}_{ss'}. \tag{31}$$

The structure (30) follows from detailed derivations, however, heuristically one can argue that this structure is needed to keep track of the time of *measurement* t in addition to the times where the incoming and outgoing electrons are scattered, t_1 and t_2 (see the Feynman diagrams in Fig. 2). Although the current

vertex still has a four-leg structure, just as the vertex, due to its double time dependence it can no longer be identified with the coupling vertex. Therefore we represent it by a different diagrammatic symbol, depicted in Fig. 2.

To investigate how the current vertex is renormalized, we follow a strategy similar to that of Sec. II B. We expand the generating functional (29) simultaneously in the field $h_\alpha^{(\kappa)}(t)$ and also in the interaction kernel $\mathbf{g}(t)$. Again, similar to Sec. II, we find that changing $a \to a'$ changes only the contributions of those diagrams and those configurations, where (at least) two contracted fields are close to each other, $|t_1 - t_2| \sim a$. The contractions of the electronic fields appearing in a current vertex can then be classified similar to Fig. 4, and one can argue that only contractions shown in Fig. 9 must be considered, with both the current and the interaction vertex lying on the same branch of the Keldysh contour. Notice that the current and the coupling vertex are not equivalent and therefore do not "commute" when placed on one of the branches of the Keldysh contour. Therefore the number of diagrams for the upper branch of the Keldysh contour is four. These diagrams are sketched in Fig. 9.

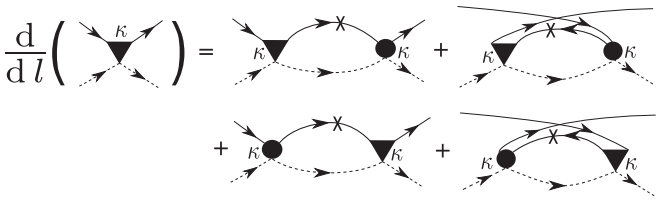

FIG. 9. Diagrams renormalizing the current vertex. Crosses indicate the logarithmic derivative with respect to the scaling parameter a. Notice that the current and the coupling vertex do not "commute" and the diagrams came in pairs. Each diagram corresponds to a term in Eqs. (32) and (33).

The RG equations of the current vertex can be obtained following very similar lines as in Sec. II, and we obtain for the left current vertex, $V_{\alpha\alpha'}^{\sigma s;\sigma' s'} \equiv (V^L)_{\alpha\alpha'}^{\sigma s;\sigma' s'}$,

$$\begin{aligned}\frac{dV_{\alpha\alpha'}^{\sigma s;\sigma' s'}(t-\tilde{t},\tilde{t}-t')}{dl} = \sum_{\tilde{\alpha},\tilde{s},\tilde{\sigma}} \int dt_1\, dt_2 \Bigg[& g_{\alpha\tilde{\alpha}}^{\sigma s;\tilde{\sigma}\tilde{s}}(t-t_1) V_{\tilde{\alpha}\alpha'}^{\tilde{\sigma}\tilde{s};\sigma' s'}(t_2-\tilde{t},\tilde{t}-t') \frac{\partial G_{\tilde{\alpha}}^t(t_1-t_2)}{\partial l} F_{\tilde{s}}^t\left(\frac{t+t_1}{2}-\tilde{t}\right) e^{i\lambda_s(t+t_1-2\tilde{t})/2} \\ & + g_{\alpha\tilde{\alpha}}^{\sigma\tilde{s};\tilde{\sigma}s'}(t-t_1) V_{\tilde{\alpha}\alpha'}^{\tilde{\sigma}s;\sigma'\tilde{s}}(t_2-\tilde{t},\tilde{t}-t') \frac{\partial G_{\tilde{\alpha}}^t(t_1-t_2)}{\partial l} F_{\tilde{s}}^t\left(\tilde{t}-\frac{t_1+t}{2}\right) e^{-i\lambda_{s'}(t_1+t-2\tilde{t})/2} \\ & + V_{\alpha\tilde{\alpha}}^{\sigma\tilde{s};\tilde{\sigma}s'}(t-\tilde{t},\tilde{t}-t_1) g_{\tilde{\alpha}\alpha'}^{\tilde{\sigma}s;\sigma'\tilde{s}}(t_2-t') \frac{\partial G_{\tilde{\alpha}}^t(t_1-t_2)}{\partial l} F_{\tilde{s}}^t\left(\frac{t'+t_2}{2}-\tilde{t}\right) e^{i\lambda_s(t_2+t'-2\tilde{t})/2} \\ & + V_{\alpha\tilde{\alpha}}^{\sigma s;\tilde{\sigma}\tilde{s}}(t-\tilde{t},\tilde{t}-t_1) g_{\tilde{\alpha}\alpha'}^{\tilde{\sigma}\tilde{s};\sigma' s'}(t_2-t') \frac{\partial G_{\tilde{\alpha}}^t(t_1-t_2)}{\partial l} F_{\tilde{s}}^t\left(\tilde{t}-\frac{t'+t_2}{2}\right) e^{-i\lambda_{s'}(t_2+t'-2\tilde{t})/2} \Bigg]. \end{aligned} \tag{32}$$

Again, following the same steps as in Sec. II B and approximating the cutoff function as in (17), we obtain

$$\begin{aligned}\frac{dV_{\alpha\alpha'}^{\sigma s;\sigma' s'}(\omega,\omega')}{dl} = -\sum_{\tilde{\alpha}\tilde{\sigma}\tilde{s}} \Bigg[& g_{\alpha\tilde{\alpha}}^{\sigma s;\tilde{\sigma}\tilde{s}}\left(\omega+\frac{\lambda_{s\tilde{s}}}{2}\right) V_{\tilde{\alpha}\alpha'}^{\tilde{\sigma}\tilde{s};\sigma' s'}(\omega+\lambda_{s\tilde{s}},\omega') \Xi_a^{\tilde{s}}(\omega+\lambda_{s\tilde{s}}-\mu_{\tilde{\alpha}}) \\ & + V_{\alpha\tilde{\alpha}}^{\sigma s;\tilde{\sigma}\tilde{s}}(\omega,\omega'+\lambda_{s'\tilde{s}})\, g_{\tilde{\alpha}\alpha'}^{\tilde{\sigma}\tilde{s};\sigma' s'}\left(\omega'+\frac{\lambda_{s'\tilde{s}}}{2}\right) \Xi_a^{\tilde{s}}(\omega'+\lambda_{s'\tilde{s}}-\mu_{\tilde{\alpha}}) \\ & - g_{\alpha\tilde{\alpha}}^{\sigma\tilde{s};\tilde{\sigma}s'}\left(\omega+\frac{\lambda_{\tilde{s}s'}}{2}\right) V_{\tilde{\alpha}\alpha'}^{\tilde{\sigma}s;\sigma'\tilde{s}}(\omega+\lambda_{\tilde{s}s'},\omega') \Xi_a^{\tilde{s}}(\omega+\lambda_{\tilde{s}s'}-\mu_{\tilde{\alpha}}) \\ & - V_{\alpha\tilde{\alpha}}^{\sigma\tilde{s};\tilde{\sigma}s'}(\omega,\omega'+\lambda_{\tilde{s}s})\, g_{\tilde{\alpha}\alpha'}^{\tilde{\sigma}s;\sigma'\tilde{s}}\left(\omega'+\frac{\lambda_{\tilde{s}s}}{2}\right) \Xi_a^{\tilde{s}}(\omega'+\lambda_{\tilde{s}s}-\mu_{\tilde{\alpha}}) \Bigg]. \end{aligned} \tag{33}$$

This set of equations needs be solved parallel to the scaling equations, Eq. (15) with the initial condition (31).

As we discussed before, though the renormalized couplings $\mathbf{g}(\omega)$ drive the scaling of the current vertices, $\mathbf{V}(\omega_1,\omega_2,a_0)$, there seems to be no simple connection between these two. In other words, it is unavoidable to introduce the renormalized current vertices within the functional RG scheme to compute time-dependent current correlations. Very importantly, the above extension also solves to problem of *current conservation*: Eq. (33) is linear in $\mathbf{V}$. Therefore, as the bare vertices satisfy $\mathbf{v}_L = -\mathbf{v}_R$, the full vertices shall also satisfy $\mathbf{V}_L(t,t') = -\mathbf{V}_R(t,t')$ by construction, and therefore the condition $I_L^{(\kappa)}(t) + I_R^{(\kappa)}(t) \equiv 0$ is automatically fulfilled for any value of the cutoff, a. On the other hand, we could not find any systematic way to generate a current field from just the renormalized action, Eq. (8), such that it respected current conservation. The introduction of the current vertex and its RG equation seem to be therefore unavoidable to extend the formalism of Refs. [17,30] to compute time-dependent correlations.

Figure 10 displays the frequency dependence of the $\uparrow\uparrow;\uparrow\uparrow$ component for a fixed bias voltage, in the absence/presence of the external magnetic field. Similar to the renormalized couplings, the components of the current vertex display logarithmic singularities in the frequency space at $\omega = \pm V/2$. These singularities get shifted in the presence of the external magnetic field.

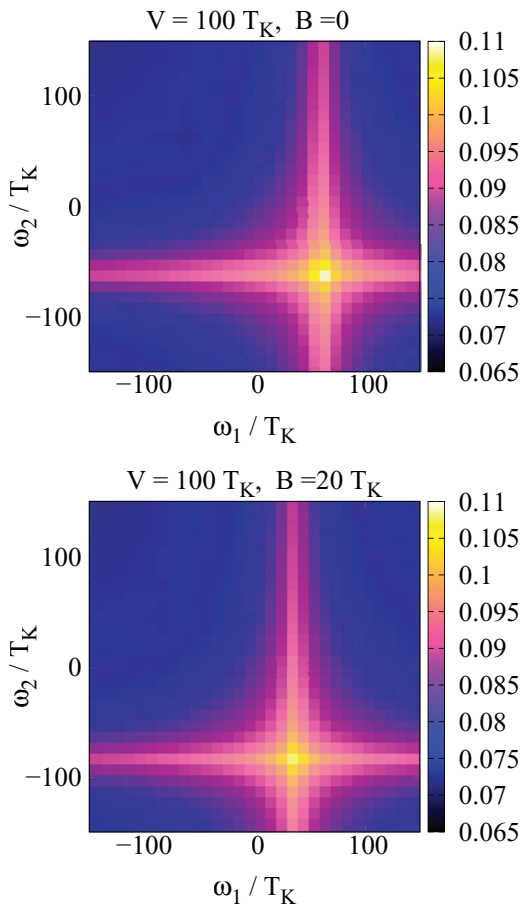

FIG. 10. (Color online) Frequency dependence of the current vertex kernel $V_{LR}^{\uparrow\uparrow;\uparrow\uparrow}(\omega_1,\omega_2)$ for a fixed voltage bias $V = 50\ T_K$, and for magnetic field $B = 0$ (top) and $20\ T_K$ (bottom). In the absence of an external field it shows a logarithmic singularity at frequencies $\hbar\omega \simeq \pm eV/2$, which is then shifted by the presence of the external magnetic field.

IV. DECOHERENCE EFFECTS

Let us now turn to the important issue of decoherence. Under nonequilibrium circumstances, a large bias voltage necessarily entails a finite spin lifetime and related decoherence effects, as also observed experimentally [5,46]. These decoherence effects lead to a natural low energy cutoff for the logarithmic singularities and the renormalization group flow. In this section, we try to capture spin relaxation within two different approaches. First, we use a perturbative master equation method with renormalized couplings to determine the voltage and temperature dependence of the Korringa spin relaxation rate, $\Gamma_K(T,V)$. Then, in Sec. IV 2, we compute the pseudofermion's relaxation rate, $\Gamma_{\rm pf}(V,T)$. Both approaches result in a consistent picture when combined self-consistently with the RG scheme developed in Secs. II and III.

1. Korringa relaxation rate: a master equation approach

In the perturbative regime, $\min\{T,eV,B\} \gg T_K$, one can investigate the relaxation of the spin by perturbation theory. In this parameter range, spin-flip events are rare, and they can be treated as a Markov process [47]. The scattering events in this Markov process are generated by the exchange interaction, and consist of the scattering of an electron with spin σ' from lead β into a final state of spin σ in lead α, while flipping the impurity spin from s' to s. To leading order in perturbation theory, the transition rate for such process $\gamma_{\alpha\leftarrow\beta}^{\sigma s\leftarrow\sigma' s'}$, is given by the simple Fermi golden rule expression

$$\gamma_{\alpha\leftarrow\beta}^{\sigma s\leftarrow\sigma' s'} \approx \frac{\pi}{2}\int d\omega\, |j_{\alpha\beta}\,\boldsymbol{\sigma}_{\sigma\sigma'}\,\mathbf{S}_{ss'}|^2\,\bar{f}_\alpha(\omega+\lambda_{ss'})f_\beta(\omega) \tag{34}$$

with $f_\alpha(\omega) = f(\omega-\mu_\alpha)$ the shifted Fermi-Dirac distribution for the electrons in the lead α, and $\bar{f}_\alpha(\omega) = 1 - f_\alpha(\omega)$. Notice the shift in the energy of the conduction electrons by $\lambda_{ss'} = -(s-s')B/2$ in the argument due to energy conservation. Within this simple master equation approach, it then follows that the spin decays exponentially,

$$\langle S_z\rangle \propto \exp[-(\Gamma_\Uparrow + \Gamma_\Downarrow)t] \tag{35}$$

with

$$\Gamma_\Uparrow = \sum_{\alpha,\beta,\sigma,\sigma'} \gamma_{\alpha\leftarrow\beta}^{\sigma\Uparrow\leftarrow\sigma'\Downarrow} \quad\text{and}\quad \Gamma_\Downarrow = \sum_{\alpha,\beta,\sigma,\sigma'} \gamma_{\alpha\leftarrow\beta}^{\sigma\Downarrow\leftarrow\sigma'\Uparrow}. \tag{36}$$

This allows us to identify the Korringa relaxation rate

$$\Gamma_K(T,eV,B) = \Gamma_\Uparrow + \Gamma_\Downarrow, \tag{37}$$

as the relevant decoherence rate in the problem.

The integrals (34) can be evaluated analytically. In the limit of large voltages, $eV \gg T,B$, e.g., Γ_K assumes a simple analytical form:

$$\Gamma_K(T,eV\gg B) \approx \pi T\left(j_{LL}^2 + j_{RR}^2\right) + j_{LR}^2\, eV\, \coth\left(\frac{eV}{2T}\right) + \mathcal{O}(B^2). \tag{38}$$

For large magnetic fields, on the other hand, $B \gg eV$, we obtain

$$\Gamma_K(T,eV\ll B) = \pi\frac{B}{2}\left(j_{LL}^2 + j_{RR}^2 + 2j_{LR}^2\right)\coth\left(\frac{B}{2T}\right) + \mathcal{O}(eV^2). \tag{39}$$

It is instructive to express the Korringa rate in terms of the anisotropy angle, θ, introduced in Eq. (20). In the limit when one of the variables T, B, or V is much larger than the other two we obtain:

$$\Gamma_K = \begin{cases} \pi j^2 T & (B,V\to 0), \\ \frac{1}{4}\pi j^2 |eV|\sin^2(\theta) & (T,B\to 0), \\ \frac{1}{2}\pi j^2 |B| & (T,V\to 0). \end{cases} \tag{40}$$

These results agree with those of Refs. [12,48,49]. Notice that the temperature and the magnetic field generate a decoherence rate independent of the asymmetry, while the voltage-induced spin relaxation rate depends on the asymmetry. This is not so surprising since the current flowing through the device is proportional to $\sim\sin^2(\theta)$, and is suppressed for a strongly asymmetrical quantum dot. The Korringa rate in the large voltage limit is directly proportional to this current and thus strongly depends on the asymmetry θ.

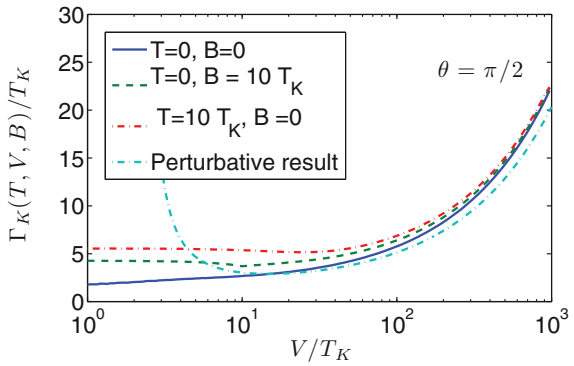

FIG. 11. (Color online) The voltage dependence of Korringa rate for different temperatures and magnetic fields. The dashed (blue) line represents the perturbative result: $\Gamma_K(eV \gg B,T) = \pi|eV|/4\ln^2(|eV|/2T_K)$.

The previous results were obtained to lowest order in the exchange coupling, $j_{\alpha\beta}$. Higher-order logarithmic corrections can be summed up perturbatively [48,49]. We can estimate the size of these corrections by simply replacing the bare coupling j with its renormalized value, $j \to 1/\ln(\max(|eV|,|B|,T)/T_K)$. This approximation, however, breaks down at $V \approx 10\,T_K$. In order to approach the regime $V \approx T_K$, the self-consistent incorporation of the relaxation rate $\Gamma_K(V)$ is necessary [7]. In particular, in the FRG scheme we follow Ref. [48] to express the running value of the relaxation rate $\Gamma_K(a)$ as

$$\Gamma_K(a) = 2\pi \sum_{\alpha\beta\sigma\sigma'} \sum_{s\neq s'} \int d\omega \left| g_{\alpha\beta}^{\sigma s;\sigma' s'}\left(a,\omega+\frac{\lambda_{ss'}}{2}\right)\right|^2 \times f_\alpha(\omega+\lambda_{ss'}) f_\beta(\omega). \tag{41}$$

The physical Korringa rate Γ_K is then obtained by solving the RG equation self-consistently with the cutoff function (17) and taking the $a \to 0$ limit.

In Figs. 11 and 12, we compare the voltage and temperature dependence of the Korringa rates as computed perturbatively and by the FRG method. Clearly, for $V \gg T_K$ the perturbative result gives a good estimate, but the result starts to deviate below $V \simeq 10\,T_K$, and for $V \approx T_K$ a self-consistent calculation of Γ_K is necessary. The physical explanation of the much better performance of FRG is simple: approaching T_K the effective exchange rate becomes large. This, however, generates an increased spin relaxation rate, which then naturally feeds back and provides a cutoff for the logarithmic divergency.

Notice that our real-time FRG results are restricted to the region where at least one of the parameters T, eV, or $|B|$ is somewhat larger than T_K. Therefore the $B = T = 0$ FRG curve in Fig. 11 (the $V = B = 0$ FRG curve in Fig. 12) should be considered wit a grain of salt for voltages $|eV| \sim T_K$ (temperatures $T \sim T_K$).

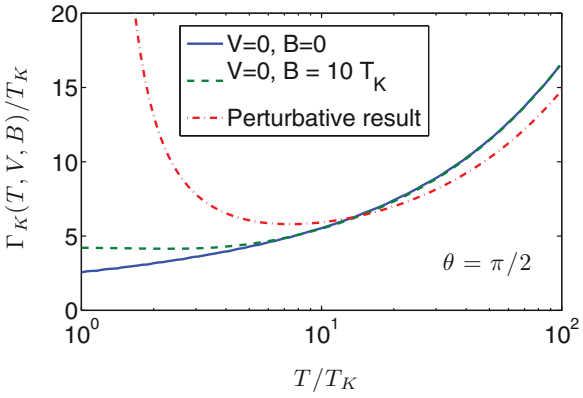

FIG. 12. (Color online) The temperature dependence of the Korringa rate for V = 0. The dashed-dotted (red) line represents the perturbative result: $\Gamma_K(T \gg eV,B) \simeq \pi\,T/\ln^2(T/T_K)$.

2. Pseudofermion self-energy and lifetime

Within the FRG scheme, one often identifies the pseudofermion relaxation rate $\Gamma_{\rm pf}$ as the low-energy cutoff energy of the scaling [50]. Although this energy scale—being related to the lifetime of a slave particle—has no direct physical meaning, neverheless, it appears naturally in the FRG scheme [see Eq. (17)], and is directly related to the spin relaxation rate. The rate $\Gamma_{\rm pf}$ can be most easily defined as the imaginary part of the retarded pseudofermion self-energy, which can also be expressed in terms of the bigger and lesser pseudofermion self-energies as

$$\Gamma_{\rm pf} = \frac{i}{2}\sum_s \lim_{\omega\to\lambda_s} (\Sigma_s^>(\omega) - \Sigma_s^<(\omega)). \tag{42}$$

The second-order FRG diagrams for $\Sigma_s^{\lessgtr}$ are shown in Fig. 13. The leading-order (perturbative) expression of $\Gamma_{\rm pf}$ can be obtained by using the bare exchange couplings,

$$\Gamma_{\rm pf}^{(0)} = \frac{\pi}{8}\sum_{\alpha,\beta}\sum_{i,s,s'}\int d\omega\,|S^i_{ss'}|^2 |j_{\alpha\beta}|^2\,\bar f_\beta(\omega)\,f_\alpha(\omega-\lambda_{ss'}). \tag{43}$$

Evaluating Eq. (43) in the asymptotic limit, when again one of the variables T, V, B is much larger that the other ones, we find that $\Gamma_{\rm pf}^{(0)} = (3/8)\,\Gamma_K^{(0)}$, with $\Gamma_K^{(0)}$ the leading-order expression of the Korringa rate, Eq. (37).

The complete expression of the running rate, $\Gamma_{\rm pf}(a)$ is somewhat involved, and can be expressed as

$$\Gamma_{\rm pf}(a) = \frac{\pi}{2}\sum_{\alpha\beta\sigma\sigma'}\sum_{ss'}\int d\omega\, g_{\alpha\beta}^{\sigma s;\sigma' s'}\left(a,\omega-\frac{\lambda_{ss'}}{2}\right)\bar f_\beta(\omega)\, g_{\beta\alpha}^{\sigma' s';\sigma s} \times \left(a,\omega-\frac{\lambda_{ss'}}{2}\right) f_\alpha(\omega-\lambda_{ss'}). \tag{44}$$

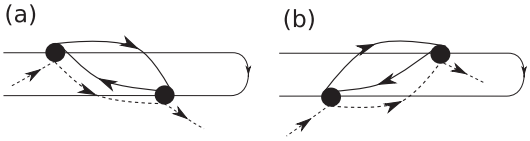

FIG. 13. Second-order diagrams for the Keldysh components of the self-energy. In (a), we represent $\Sigma^>(t)$, while in (b), $\Sigma^<(t)$ is diplayed.

Similar to Γ_K, the renormalized rate $\Gamma_{\rm pf}$ can be obtained by solving the RG equations self-consistently [now using $\Gamma_{\rm pf}(a)$ as a cutoff], and then taking the $a \to 0$ limit.

It is a delicate problem by itself to decide which of the two rates, Γ_K and $\Gamma_{\rm pf}$ should be used as an infrared cutoff. This issue has been discussed in detail in Ref. [48], by doing pertubative calculations up to third order in j. This analysis shows that in the expression for the conduction electrons T matrix, e.g., several logarithmic singularities emerge which are cut off by different rates. Since Γ_K and $\Gamma_{\rm pf}$ differ only by a numerical prefactor of order 1, here we shall not distinguish them and we choose to use the physical spin relaxation rate Γ_K as an infrared cutoff, similar to Ref. [9].

V. FINITE-FREQUENCY NOISE

As mentioned earlier, the current operator, $\hat{I}_\alpha(t)$, does not commute with itself at different times, and therefore, several different current-current correlators can be defined (see Sec. III A). Emission and absorption noise measurements, e.g., give access to the "bigger" correlation function,

$$S^{>}_{\alpha\beta}(\omega) = \int_{-\infty}^{\infty} dt\; e^{i\omega t} S^{>}_{\alpha\beta}(t) \tag{45}$$

with $S^{>}_{\alpha\beta}(t)$ defined in Eq. (25). The spectrum $S^{>}_{\alpha\beta}(\omega)$ is in general a complex, not symmetrical function in frequency. As discussed in Ref. [45], $S^{>}(\omega)$ can be interpreted as the rate by which the system absorbs ($\omega > 0$) or emits ($\omega < 0$) photons of energy $|\hbar\omega|$. While usual amplifiers measure a combination of emission and absorption processes, using a *quantum detector* gives the opportunity to measure separately the emission and absorption noise. Depending on whether photons are emitted or absorbed by the quantum detector, one can thus measure the $\omega < 0$ (emission) or the $\omega > 0$ (absorption) part of $S^{>}(\omega)$ [51],

$$S^{\rm em/ab}_{\alpha\beta}(\omega > 0) \equiv S^{<}_{\alpha\beta}(\pm\omega). \tag{46}$$

Time-dependent current-current correlation functions may depend not only on the way noise is measured, but also on the precise spatial location (electrode) where currents are measured. In our case, however, current conservation [Eq. (23)] guarantees that it is enough to focus only on one noise component, say $S^{\gtrless}_{LL}$, as all the other ones are trivially related to it,

$$S^{\gtrless}_{RR}(\omega) = -S^{\gtrless}_{LR}(\omega) = S^{\gtrless}_{LL}(\omega)\,. \tag{47}$$

We shall therefore focus on $S^{\gtrless}_{LL}$ in what follows.

A real-time diagrammatic representation of the noise correlation functions, Eqs. (25) and (26) is presented in Fig. 14.

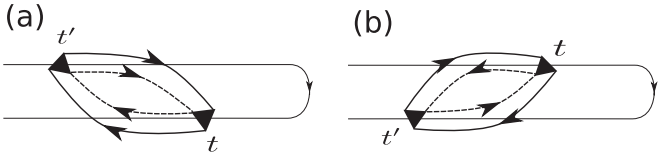

FIG. 14. Diagrams for the noise components. $S^{>}(t,t')$ is represented in (a), and $S^{<}(t,t')$ in (b).

Using Eq. (30), the spectra $S^{\gtrless}_{LL}$ can be obtained via Fourier transformation

$$S^{>}_{LL}(\omega) = \frac{e^2}{16}\sum_{ss'} p_s \sum_{\alpha\alpha'\sigma\sigma'} \int d\tilde{\omega}\; V^{\sigma s;\sigma' s'}_{\alpha\alpha'}(\tilde{\omega}_-,\tilde{\omega}_+) \times G^{>}_{\alpha'}(\tilde{\omega}_+)\, V^{\sigma' s';\sigma s}_{\alpha'\alpha}(\tilde{\omega}_+,\tilde{\omega}_-)\, G^{<}_{\alpha}(\tilde{\omega}_-), \tag{48}$$

$$S^{<}_{LL}(\omega) = \frac{e^2}{16}\sum_{ss'} p_s \sum_{\alpha\alpha'\sigma\sigma'} \int d\tilde{\omega}\; V^{\sigma s;\sigma' s'}_{\alpha\alpha'}(\tilde{\omega}_-,\tilde{\omega}_+) \times G^{<}_{\alpha'}(\tilde{\omega}_+)\, V^{\sigma' s';\sigma s}_{\alpha'\alpha}(\tilde{\omega}_+,\tilde{\omega}_-)\, G^{>}_{\alpha}(\tilde{\omega}_-)\,, \tag{49}$$

with $\tilde{\omega}_\pm = \tilde{\omega} \pm \omega/2 \pm \lambda_{ss'}/2$, $G^{\gtrless}_{\alpha}(\omega)$ the electronic Green's functions, and p_s the probability of the spin (pseudofermion) being in state s. These latter are computed self-consistently in terms of the transition rates, Γ_s, by solving the detailed balance equation, $p_\Uparrow \Gamma_\Downarrow = p_\Downarrow \Gamma_\Uparrow$.

A. Emission noise spectra

In the experiments of Ref. [5], one measures the emission noise of a nanocircuit at a fixed frequency, ω, as a function of the bias voltage, $S^{\rm em}(\omega, V)$. In Fig. 15, we therefore display

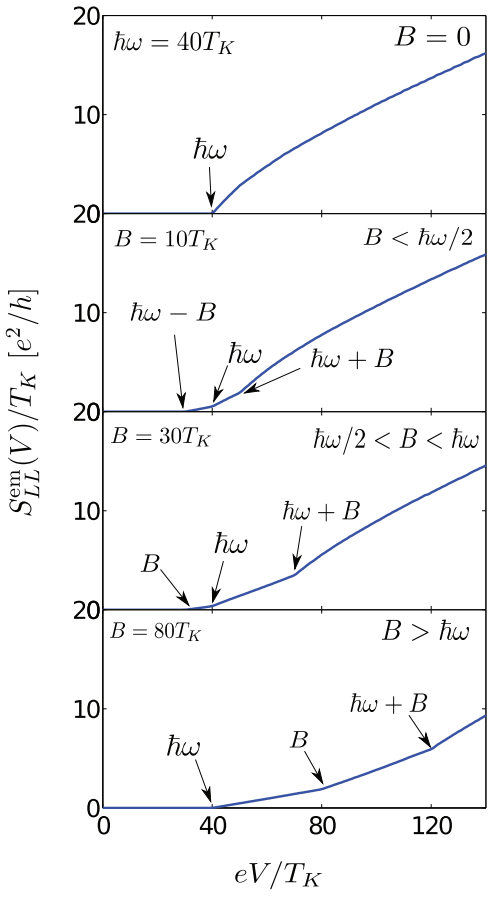

FIG. 15. (Color online) Voltage dependence of the emission noise $S^{\rm em}_{LL}(\omega)$ for a fixed frequency, $\omega = 40\,T_K$, and for different values of the magnetic field. The arrows indicate the positions of the kinks in the spectra.

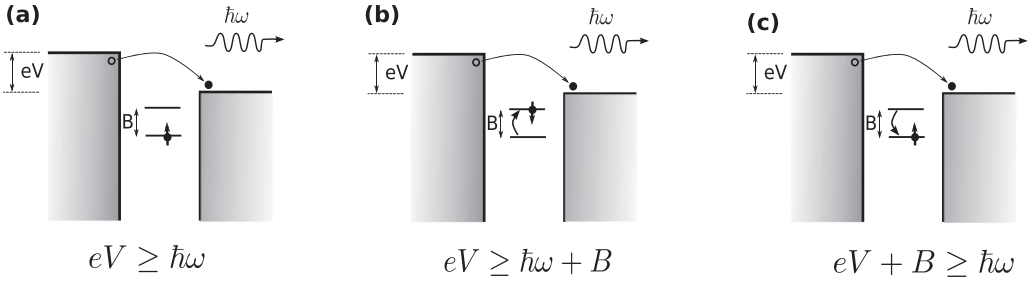

FIG. 16. Basic photon emission processes.

the zero-temperature voltage dependence of the QD's emission noise at a fixed finite frequency $\omega = 40\,T_K$ for various external magnetic fields. The spectra develop kinks (appearing as sharp steps in $dS^{\rm em}/dV$, as shown in the introduction), associated with the opening of various new photon-emission channels, displayed in Fig. 16. These kinks can be understood as follows.

In the absence of an external field, $B = 0$, there is a single kink (threshold), located at $\hbar\omega/e$. Below this voltage the energy gain of an electron passing through the circuit is not enough to trigger photon emission. Above this threshold, on the other hand, the emission noise exhibits a sharp increase followed by a less steep, close to linear dependence at larger voltages, $V \gg T_K$. The sharp increase close to threshold is a manifestation of the nonequilibrium Kondo effect [5] and amounts to a a peak in the $dS^{\rm em}/dV$ spectrum, as also observed experimentally [5].

For small magnetic fields, $B < \hbar\omega/2$ two more kinks appear at $V = \hbar\omega \pm B$ (see second panel of Fig. 15). These can be understood as follows. For very small voltages, the spin is polarized by the external filed ($p_{\Uparrow} = 1,\ p_{\Downarrow} = 0$). Once the voltage becomes larger than the splitting of the two spin states, B, spin-flip processes can populate the state $|\Downarrow\rangle$, and $p_{\Downarrow}$ becomes finite. Therefore photon emission becomes possible through spin-flip processes (shown in Fig. 16), once the voltage reaches the threshold $eV = \hbar\omega - B$. Conversely, a new spin-flip scattering channel opens at $eV = \hbar\omega + B$, where the potential energy gain of an electron passing through the QD is converted to a spin excitation and the energy of the emitted photon [see Fig. 16(b)].

The situation explained in the previous paragraph changes slightly, once the magnetic field becomes somewhat larger that $\hbar\omega/2$ [see Fig. 16(c)]. In this case, $p_{\Downarrow}$ remains zero as long as $eV < B$. However, spin-flip emission becomes energetically possible immediately once the voltage reaches B and thus $p_{\Downarrow}$ becomes nonzero, since in this case, the voltage bias automatically satisfies the condition $eV > B > \hbar\omega - B$. Correspondingly, we recover three kinks at $eV = B$, $eV = \hbar\omega$, and $eV = \hbar\omega + B$, the latter kink corresponding the simultaneous photon emission and $\Uparrow \to \Downarrow$ spin-flip process. Finally, for $B > \hbar\omega$, the location of the kinks remains the same as for $\hbar\omega/2 < B < \hbar\omega$, but in this case emission starts at the "optical gap," $\hbar\omega$.

Though the features discussed so far seem to be relatively weak, experimentally one has access to the differential noise spectrum, i.e., to the derivative of the current noise with respect to the voltage, $dS^{\rm em}(V)/dV$ [5]. This quantity, already presented in Fig. 1 displays much sharper features than $S^{\rm em}(V)$ itself at every threshold, and should allow to identify each process unambiguously.

B. Frequency dependence of $S^{>}(\omega)$ and $S^{s}(\omega)$

So far, we only discussed the behavior of $S^{>}(\omega)$ at a fixed negative frequency (emission noise), as a function of external voltage. The spectrum $S^{>}(\omega)$ at a finite and fixed *voltage* contains, however, more information since it accounts both for absorption and for emission processes. The function $S^{>}(\omega)$ is displayed in Fig. 17 for various magnetic fields.

The structures on the $\omega < 0$ (emission) side can be understood along lines very similar to the ones presented in the

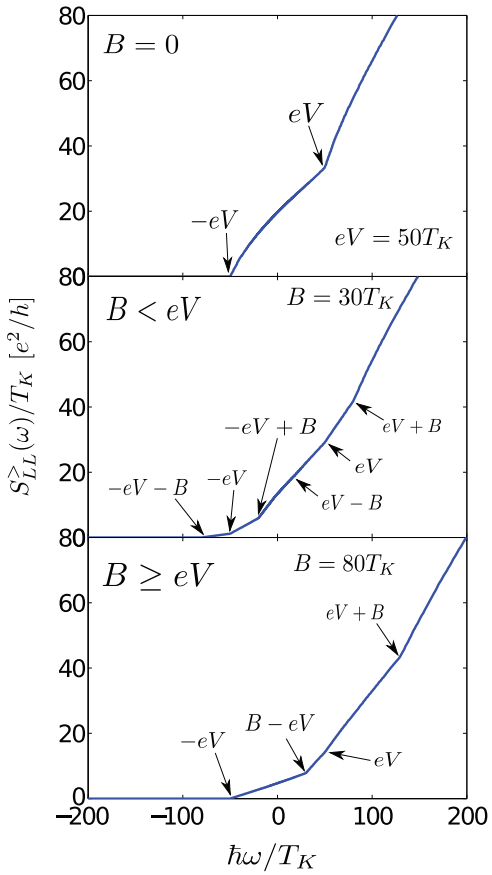

FIG. 17. (Color online) Frequency dependence of the bigger noise $S^{>}_{LL}(\omega)$ at $T = 0$ and for different values of the magnetic field. The arrows indicate the corresponding frequency at which weak logarithmic singularities emerge in the spectra.

previous section. Here, however, we need to distinguish only two regions. For $eV < B$, the spin-down state is not populated. Therefore, in this region, only photons with energy $\hbar\omega < eV$ are emitted in a process where an electron is transferred through the QD without spin flip. Correspondingly, in this region, there is only an emission threshold at $\hbar\omega = -eV$ (see third panel of Fig. 17). For $eV > B$, on the other hand, the spin $\Downarrow$ state of the QD gets populated, and all three emission processes of Fig. 15 become active. Correspondingly a threshold is shifted to $\omega = -(eV + B)$ and two more kinks appear at frequencies $\hbar\omega = -eV$ and $\omega = -(eV - B)$.[5]

Understanding the $\omega > 0$ (absorption) side is much easier. There, all three absorption processes are allowed (if the photon's energy is large enough), and correspondingly, three kinks are always recovered at frequencies $\hbar\omega = eV$ and $\omega = |eV \pm B|$.

The structure of the symmetrized noise, measured by a conventional amplifier is much simpler: since the symmetrized noise is just a combination of the "bigger" and "lesser" noises $S^s(\omega) = [S^>(\omega) + S^<(\omega)]/2$, the kinks associated with the thresholds of the various absorption and emission processes appear now in it symmetrically at all three frequencies, $\hbar\omega = \pm eV$ and $\omega = \pm(eV \pm B)$ (see Fig. 18).

[5]Throughout this discussion we assume $eV, B > 0$.

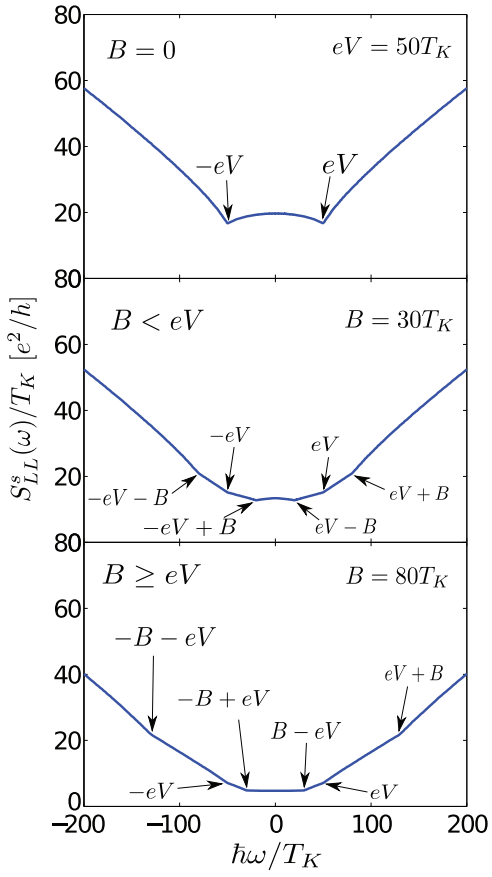

FIG. 18. (Color online) Frequency dependence of the symmetric noise $S^s_{LL}(\omega)$ at $T = 0$ and for different values of the external magnetic field as computed with the RTFRG.

VI. CONCLUSIONS

In this work, we have developed in detail a real-time functional renormalization group (FRG) formalism, originally proposed in Ref. [6], and used it to study the finite-frequency noise in a quantum dot, subject to an external magnetic field in the local moment regime. We have shown that within a systematic real-time FRG formalism, similar to the interaction vertex, the current vertex necessarily becomes nonlocal in time, and a RG equation must be constructed to account for the renormalization of the current vertex. The structure of our real-time RG scheme thus resolves the long-standing problem of current conservation. Our approach sums up all leading logarithmic contributions and is valid at any frequency, ω, voltage eV, or magnetic field B, provided that $\max\{\omega, eV, B\} \gg T_K$. As demonstrated in Ref. [5], the present theory accounts well for the features observed experimentally.

We have solved the FRG equations in Fourier space numerically, and computed the emission/absorption and symmetrized noise spectra through a voltage biased QD. A very rich behavior is found. In the differential emission noise of the QD $dS^{\rm em}(\omega, V)/dV$ (measured at a finite frequency ω), logarithmic singularities appear at the thresholds, $\hbar\omega = eV$ and $\hbar\omega = |eV \pm B|$, corresponding to the opening of spin-conserving and spin-flip emission channels, and reflecting the presence of the nonequilibrium Kondo effect. The experimentally measured peaks (anomalies) in the differential emission spectra of Ref. [5], $dS^{\rm em}/dV$ are thus predicted to split up in a magnetic field into two or three singular features (steps), as shown in Fig. 1. These results agree in large with the ones presented in Ref. [39], where similar quantities were investigated by using a somewhat different (and more involved) technique, formulated in terms of a Liouvillian approach on the Keldysh contour. Though the results (locations and general structure of dS/dV anomalies, etc.) of the two approaches are rather similar, there are, however, some differences, too, worth mentioning. Maybe the most important difference between the method of Ref. [39] and ours is the way the two formalisms treat spins and spin relaxation. While our approach is based upon a pseudofermion formalism, the computations of Ref. [39] are carried out directly in terms of the impurity spin. A great advantage of the pseudofermion approach discussed here is that it allows a systematic and relatively easy computation of the dynamical vertex function, and systematically incorporates dynamical logarithmic corrections. Including spin relaxation, however, is not entirely straightforward within this approach. In a magnetic field in the z direction, e.g., the spin acquires a finite expectation value, $\langle S^z(t)\rangle \neq 0$. Correspondingly, the spin-spin correlation function $\langle S^z(t)S^z(0)\rangle$ does not decay to zero, and its Fourier transform therefore contains a delta peak at $\omega = 0$. As argued in Ref. [52], in equilibrium, this amounts in the appearance of purely elastic scattering processes in a magnetic field, originally absent for $B = 0$. At a finite bias, if indeed still present, such elastic left-right charge transfer processes could give rise to a sharp step in the dS/dV curves at $\omega = eV$. Indeed, such a sharp step was found at $\omega = eV$ within the approach of Ref. [39] at $T = 0$ temperature, while the other steps were found to be washed out due to spin relaxation.

Reproducing the previously mentioned finite step—if it indeed exists—is far from trivial within the pseudofermion approach. In its simpler form (where certain vertex corrections are neglected), the pseudofermion method incorporates spin relaxation only through the pseudofermion's lifetime, and, correspondingly, it predicts a broadened resonance even at $\omega = eV$. In Figs. 15–18, for simplicity, we neglected the pseudofermion's lifetime within the pseudofermion loop of Fig. 14 and approximated it by a nondecaying spin relaxation function. As shown in Fig. 1, incorporating the pseudofermion's self-consistently determined lifetime in this diagram gives a small, but finite width to all steps in the dS/dV curves. One could, of course, replace this loop—somewhat heuristically—by a resumed pseudofermion ladder series (and thereby reproduce the nondecaying part of the spin-spin correlation function), but we preferred to present here a self-consistent framework. Whether the finite jump at $\omega = eV$—obtained within a perturbative approach of Ref. [39]—indeed survives in a biased system is a rather nontrivial, intriguing question. Observing it seems to be, unfortunately, beyond current experimental resolution.

Finally, we should emphasize that the method presented here is not only relatively easy, but also quite general. It is not just restricted to a QD, but can be used for *any* system with some localized degrees of freedom, coupled to conduction electrons/leads via a Kondo-like coupling, Eq. (2). It is thus straightforward to apply it to molecular singlet triplet transitions [53], double quantum dots systems [54–56], or side-coupled molecules [57], and a variety of strongly correlated nanostructures.

ACKNOWLEDGMENTS

We would like to thank S. Andergassen, J. Basset, H. Bouchiat, R. Deblock, M. Pletyukhov, and H. Schöller for interesting discussions. This research has been supported by the French-Roumanian Grant DYMESYS (ANR 2011-IS04-001-01 and PN-II-ID-JRP-2011-1) and by the Hungarian Research Funds under Grant Nos. K105149, CNK80991. C.-H.C. acknowledges the support from NSC Grant Nos. 98-2918-I-009-06, 98-2112-M-009-010-MY3, 101-2628-M-009-001-MY3 the NCTU-CTS, the MOE-ATU program, the NCTS of Taiwan, Republic of China.

APPENDIX: GREEN'S FUNCTIONS

Evaluation of the path integrals gives automatically products of operators ordered along the Keldysh contour. Correspondingly, the average $-i\langle\psi^{(2)}_{\alpha\sigma}(t)\bar{\psi}^{(1)}_{\alpha'\sigma'}(t')\rangle_S$, e.g., yields the operator product $-i\langle\psi_{\alpha\sigma}(t)\bar{\psi}^{\dagger}_{\alpha'\sigma'}(t')\rangle = G^{>}_{\alpha\sigma;\alpha'\sigma'}(t-t')$. Using the representation $\psi_{\alpha\sigma}(t) = \int d\xi\, c_{\alpha\sigma}(\xi)\, e^{-it(\xi+\mu_\alpha)} e^{-a|\xi|/2}$ this immediately yields, e.g.,

$$G^{(21)}_{\alpha\sigma;\alpha'\sigma'}(t) = G^{>}_{\alpha\sigma;\alpha'\sigma'}(t) = -i\delta_{\alpha\alpha'}\delta_{\sigma\sigma'} e^{-i\mu_\alpha t} \int d\xi\, e^{-a|\xi|}\,(1-f(\xi))\, e^{-i\xi t}.$$

The integral can be carried out at $T = 0$ temperature and yields a propagator $\sim -e^{-i\mu_\alpha t}/(t - ia)$. The other Keldysh propagators can be determined similarly. They are all diagonal in the spin and lead labels, $G^{(\kappa\kappa')}_{\alpha\sigma,\alpha'\sigma'}(t) = \delta_{\alpha\alpha}\delta_{\sigma\sigma'} G^{(\kappa\kappa')}_{\alpha}(t)$, and are given at $T = 0$ temperature by

$$G^{(11)}_{\alpha} = G^{t}_{\alpha}(t) = -\frac{e^{-i\mu_\alpha t}}{t - ia\ \mathrm{sgn}(t)},$$

$$G^{(22)}_{\alpha} = G^{\bar{t}}_{\alpha}(t) = -\frac{e^{-i\mu_\alpha t}}{t + ia\ \mathrm{sgn}(t)},$$

$$G^{(21)}_{\alpha} = G^{>}_{\alpha}(t) = -\frac{e^{-i\mu_\alpha t}}{t - ia},$$

$$G^{(12)}_{\alpha} = G^{<}_{\alpha}(t) = -\frac{e^{-i\mu_\alpha t}}{t + ia}.$$

The Abrikosov pseudofermion Green functions are diagonal, $F^{(\kappa\kappa')}_{ss'}(t) = \delta_{ss'} F^{(\kappa\kappa')}_{s}(t)$, and can be computed similar to the conduction electron propagators, by recurring to the operator representation. They are given by the following expressions:

$$F^{(11)}_{s}(t) = F^{t}_{s}(t) = -i\, e^{-i\lambda_s t}(\Theta(t) - e^{-\beta\lambda_s}\bar{\Theta}(t)) + \cdots,$$

$$F^{(22)}_{s}(t) = F^{\bar{t}}_{s}(t) = -i\, e^{-i\lambda_s t}(\bar{\Theta}(t) - e^{-\beta\lambda_s}\Theta(t)) + \cdots,$$

$$F^{(21)}_{s}(t) = F^{>}_{s}(t) = -i\, e^{-i\lambda_s t} + \cdots,$$

$$F^{(12)}_{s}(t) = F^{<}_{s}(t) = i\, e^{-i\lambda_s t} e^{-\beta\lambda_s} + \cdots,$$

with $\Theta(t)$ the Heaviside function, $\bar{\Theta}(t) = 1 - \Theta(t)$, and $\beta = 1/(k_B T)$. The dots indicate subleading corrections in $e^{-\beta\lambda_s}$, which can be dropped within the physical subspace $\sum_s f^{\dagger}_s f_s = 1$.

[1] E. Zakka-Bajjani, J. Ségala, F. Portier, P. Roche, D. C. Glattli, A. Cavanna, and Y. Jin, Phys. Rev. Lett. **99**, 236803 (2007).
[2] J. Gabelli and B. Reulet, Phys. Rev. Lett. **100**, 026601 (2008).
[3] E. Zakka-Bajjani, J. Dufouleur, N. Coulombel, P. Roche, D. C. Glattli, and F. Portier, Phys. Rev. Lett. **104**, 206802 (2010).
[4] J. Basset, H. Bouchiat, and R. Deblock, Phys. Rev. Lett. **105**, 166801 (2010).
[5] J. Basset, A. Y. Kasumov, C. P. Moca, G. Zaránd, P. Simon, H. Bouchiat, and R. Deblock, Phys. Rev. Lett. **108**, 046802 (2012).
[6] C. P. Moca, P. Simon, C. H. Chung, and G. Zaránd, Phys. Rev. B **83**, 201303 (2011).
[7] M. Pletyukhov and H. Schoeller, Phys. Rev. Lett. **108**, 260601 (2012).
[8] Y. Meir and N. S. Wingreen, Phys. Rev. Lett. **68**, 2512 (1992).
[9] A. Rosch, J. Paaske, J. Kroha, and P. Wölfle, J. Phys. Soc. Jpn. **74**, 118 (2005).
[10] J. Eckel, F. Heidrich-Meisner, S. G. Jakobs, M. Thorwart, M. Pletyukhov, and R. Egger, New J. Phys. **12**, 043042 (2010).
[11] R. M. Konik, H. Saleur, and A. W. W. Ludwig, Phys. Rev. Lett. **87**, 236801 (2001).
[12] S. Kehrein, Phys. Rev. Lett. **95**, 056602 (2005).
[13] B. Doyon and N. Andrei, Phys. Rev. B **73**, 245326 (2006).
[14] F. B. Anders, Phys. Rev. Lett. **101**, 066804 (2008).

[15] M. Pletyukhov and D. Schuricht, Phys. Rev. B **84**, 041309 (2011).
[16] S. Smirnov and M. Grifoni, New J. Phys. **15**, 073047 (2013).
[17] A. Rosch, J. Kroha, and P. Wölfle, Phys. Rev. Lett. **87**, 156802 (2001).
[18] Y. Meir and A. Golub, Phys. Rev. Lett. **88**, 116802 (2002).
[19] A. Thielmann, M. H. Hettler, J. König, and G. Schön, Phys. Rev. B **68**, 115105 (2003).
[20] E. Sela, Y. Oreg, F. von Oppen, and J. Koch, Phys. Rev. Lett. **97**, 086601 (2006).
[21] A. O. Gogolin and A. Komnik, Phys. Rev. Lett. **97**, 016602 (2006).
[22] L. G. Herrmann, T. Delattre, P. Morfin, J.-M. Berroir, B. Plaçais, D. C. Glattli, and T. Kontos, Phys. Rev. Lett. **99**, 156804 (2007).
[23] Y. Yamauchi, K. Sekiguchi, K. Chida, T. Arakawa, S. Nakamura, K. Kobayashi, T. Ono, T. Fujii, and R. Sakano, Phys. Rev. Lett. **106**, 176601 (2011).
[24] H.-A. Engel and D. Loss, Phys. Rev. Lett. **93**, 136602 (2004).
[25] M. Braun, J. König, and J. Martinek, Phys. Rev. B **74**, 075328 (2006).
[26] A. Schiller and S. Hershfield, Phys. Rev. B **58**, 14978 (1998).
[27] P. Fritsch and S. Kehrein, Ann. Phys. **324**, 1105 (2009).
[28] D. Schuricht and H. Schoeller, Phys. Rev. B **80**, 075120 (2009).
[29] P. Fritsch and S. Kehrein, Phys. Rev. B **81**, 035113 (2010).
[30] A. Rosch, T. A. Costi, J. Paaske, and P. Wölfle, Phys. Rev. B **68**, 014430 (2003).
[31] W. Metzner, M. Salmhofer, C. Honerkamp, V. Meden, and K. Schönhammer, Rev. Mod. Phys. **84**, 299 (2012).
[32] P. Kopietz and T. Busche, Phys. Rev. B **64**, 155101 (2001).
[33] H. Schoeller and J. König, Phys. Rev. Lett. **84**, 3686 (2000).
[34] N. Andrei, K. Furuya, and J. H. Lowenstein, Rev. Mod. Phys. **55**, 331 (1983).
[35] A. Tsvelick and P. Wiegmann, Adv. Phys. **32**, 453 (1983).
[36] K. G. Wilson, Rev. Mod. Phys. **55**, 583 (1983).
[37] I. Affleck and A. W. W. Ludwig, Phys. Rev. B **48**, 7297 (1993).
[38] A. C. Hewson, *The Kondo Problem to Heavy Fermions* (Cambridge University Press, Cambridge, 1993).
[39] S. Y. Müller, M. Pletyukhov, D. Schuricht, and S. Andergassen, Phys. Rev. B **87**, 245115 (2013).
[40] A. A. Abrikosov, Physics. Physique. Fizika **2**, 5 (1965).
[41] J. L. Cardy, *Scaling and Renormalization in Statistical Physics*, Cambridge Lectures Notes in Physics (Cambridge University Press, Cambridge, 1996).
[42] A. Rosch, J. Paaske, J. Kroha, and P. Wölfle, Phys. Rev. Lett. **90**, 076804 (2003).
[43] P.-M. Billangeon, F. Pierre, H. Bouchiat, and R. Deblock, Phys. Rev. Lett. **96**, 136804 (2006).
[44] R. Aguado and L. P. Kouwenhoven, Phys. Rev. Lett. **84**, 1986 (2000).
[45] U. Gavish, Y. Levinson, and Y. Imry, Phys. Rev. B **62**, R10637 (2000).
[46] J. Paaske, A. Rosch, P. Wolfle, N. Mason, C. Marcus, and J. Nygard, Nat. Phys. **2**, 460 (2006).
[47] M. Pustilnik and L. Glazman, J. Phys.: Condens. Matter **16**, R513 (2004).
[48] J. Paaske, A. Rosch, J. Kroha, and P. Wölfle, Phys. Rev. B **70**, 155301 (2004).
[49] H. Schoeller and F. Reininghaus, Phys. Rev. B **80**, 045117 (2009).
[50] H. Schmidt and P. Wolfle, Ann. Phys. **19**, 60 (2010).
[51] A. A. Clerk, M. H. Devoret, S. M. Girvin, F. Marquardt, and R. J. Schoelkopf, Rev. Mod. Phys. **82**, 1155 (2010).
[52] M. Garst, P. Wölfle, L. Borda, J. von Delft, and L. Glazman, Phys. Rev. B **72**, 205125 (2005).
[53] J. Hauptmann, J. Paaske, and P. Lindelof, Nat. Phys. **4**, 373 (2008).
[54] A. Makarovski, A. Zhukov, J. Liu, and G. Finkelstein, Phys. Rev. B **75**, 241407 (2007).
[55] J. S. Lim, R. López, G. L. Giorgi, and D. Sánchez, Phys. Rev. B **83**, 155325 (2011).
[56] A. Zazunov, A. L. Yeyati, and R. Egger, Phys. Rev. B **81**, 012502 (2010).
[57] F. Pauly, J. K. Viljas, J. C. Cuevas, and G. Schön, Phys. Rev. B **77**, 155312 (2008).